Coseismic slip and early afterslip of the 2024 Hyuganada earthquake modulated by a subducted seamount

Yuji Itoh[1]

[1]Earthquake Research Institute, The University of Tokyo, Tokyo, Japan

Key Points:

- The 2024 Hyuganada earthquake occurred at the leading edge of a seamount in the creeping megathrust due to ridge subduction
- The subducted seamount probably impeded up-dip mainshock rupture propagation and slowed up-dip afterslip migration speed
- Geodetic and seismological observations illustrated heterogeneous mechanical characteristics of megathrust in Hyuganada at an order of 10 km

Corresponding author: Yuji Itoh, `yitoh@eri.u-tokyo.ac.jp`

Abstract

Subducted rough topography complicates seismic and aseismic slip behavior. The 2024 M 7.1 Hyuganada earthquake occurred along the megathrust with ridge subduction. We inferred coseismic slip and afterslip using geodetic displacements to observationally illustrate the role of subducted seamounts in modulating seismic and aseismic slip processes. The inferred mainshock slip was confined in the down-dip of the seamount, suggesting that the seamount impeded the mainshock rupture initiated under enhanced compression. The inferred afterslip peaked at the up-dip of the mainshock peak with four aftershock clusters. Various onset timings of these clusters suggest the afterslip front migration slowed down when passing through the seamount. Little afterslip is inferred in a segment south of the mainshock, where the megathrust is somehow insusceptible to stress perturbation and seems to creep steadily across the mainshock occurrence. Our results geodetically highlight the mechanical heterogeneity of megathrust with ridge subduction at an order of 10 km.

Plain Language Summary

The 2024 Hyuganada earthquake occurred offshore Kyushu, Japan, where the oceanic Philippine Sea Plate subducts beneath the continental Amur plate with the highly variable seafloor topography called Kyushu-Palau ridge. Numerical simulations have shown that the subduction of irregular topography yields complex fault slip behavior on and around it, so we observationally imaged fault slip processes during and after the 2024 earthquake to illustrate the role of seamounts in impacting slip behavior on the natural fault. Our analysis suggested that (1) the mainshock was impeded when its slip front entered the seamount zone and (2) the post-mainshock aseismic afterslip front migrated more slowly when passing the seamount zone. We also did not identify a significant amount of slip in an along-strike neighbor segment of the mainshock slip area during the week following the mainshock. This segment is somehow insusceptible to stress loading from nearby fault slips and seems to creep steadily across the mainshock time.

1 Introduction

In Hyuganada, southwestern Japan, the Philippine Sea Plate subducts beneath the Amur plate. In contrast with off-Shikoku where few megathrust earthquakes except the great Nankai earthquake sequences have occurred (e.g., Ando, 1975; Sagiya & Thatcher, 1999), many earthquakes up to M 7.5 have frequently occurred along their interface offshore Hyuganada (Figure 1)(e.g., Yagi et al., 1998, 1999). However, further larger earthquakes (i.e., $M > 7.5$) have occurred much less frequently than expected from the convergence rate there (Ioki et al., 2023; K. Wang & Bilek, 2014). The most recent notable quake is the 2024 M_{JMA} 7.1 Hyuganada earthquake on August 8, 2024, which occurred near the rupture areas of the two 1996 Hyuganada earthquakes (M_w 6.8 and 6.7 for the October and the December events, respectively; Yagi et al., 1999) (Figure 1). Such a regional characteristic of seismogenesis has been understood as a result of the subduction of rough seafloor such as seamounts (e.g., K. Wang & Bilek, 2014). The subduction of Kyushu-Palau Ridge (KPR) on the incoming Philippine Sea Plate supports this interpretation (e.g., Arai et al., 2023; Yamamoto et al., 2013)(Figure 1a). Low margin-normal contraction and resultant low slip deficit rates during the interseismic stage (Figure 1b; T. Nishimura et al., 2018; S. Nishimura & Hashimoto, 2006; Noda et al., 2018; Okazaki et al., 2021; Sagiya et al., 2000; Sagiya, 2004; Wallace et al., 2009) support the steady creep nature of rugged plate interface due to the seamount/ridge subduction (e.g., Perfettini et al., 2010; K. Wang & Bilek, 2011, 2014).

Subducted seamounts locally modify stress distribution and thus complicate fault slip and locking behavior throughout the earthquake cycle. For example, the plate interface fault on top of the subducted seamount favors creep due to the heterogeneous stress distribution (K. Wang & Bilek, 2011). They sometimes also host afterslip (e.g., Itoh et al., 2023; Perfettini et al., 2010). In contrast, compressional stress and drainage along the megathrust are enhanced at the leading flank of subducted seamounts, which provides a favorable condition for ordinary earthquake generations (Ruh et al., 2016; Sun et al., 2020). Creeping subducted seamounts may impede earthquake rupture approaching them as a soft barrier (K. Wang & Bilek, 2011). Such a contrast in slip modes on and around subducted seamounts clearly explains the spatial separation of ordinary and slow earthquake activities on and around a subducted seamount offshore Ibaraki, northeastern Japan (Kubo & Nishikawa, 2020; Mochizuki et al., 2008). The 2024 mainshock epicenter and the two 1996 events are located within the subducted KPR inferred from a low seismic velocity layer near the plate interface (Yamamoto et al., 2013) (Figure 1). Within this wide zone having possible geometrical irregularities, a local seamount, inferred from local high reduced-to-pole (RTP) magnetic anomaly (Arai et al., 2023; Okino, 2015), is located at the up-dip extension of the two 1996 rupture areas and the 2024 epicenter (Figure 1a). Therefore, the 2024 event and its afterslip give us a valuable opportunity to investigate the mechanical link between seismic/aseismic fault slip and the subducted KPR, particularly, the up-dip seamount. Hence, in this study, we derive the coseismic slip and 1-week afterslip of the 2024 Hyuganada earthquake using Global Navigation Satellite System (GNSS) data to image the interlaced seismic and aseismic slip patches. Then, by comparing them with aftershocks and the subducted seamount location, we observationally illustrate the role of seamounts in modulating the dynamics of the coseismic slip and early afterslip behavior. Furthermore, we discuss the mechanical heterogeneity in Hyuganada by juxtaposing the coseismic slip and early afterslip with background seismicity and slow earthquakes.

2 Data analysis and slip inversion

2.1 GNSS data analysis

We employed GNSS coordinate time series processed by the Nevada Geodetic Laboratory (Blewitt et al., 2018) to derive coseismic and postseismic displacements associated with the 2024 Hyuganada earthquake (Figures S1-S4). First, we estimated coseismic displacements using time series at an interval of 5 minutes to minimize postseismic deformation contaminated in the coseismic displacement (Figure 2b, d, and f). We skipped the removal of multipath (Choi et al., 2004; Itoh & Aoki, 2022; Ragheb et al., 2007) and common mode errors (Wdowinski et al., 1997) for the subdaily time series because we are interested in only an instantaneous displacement step. Next, we estimated coseismic and postseismic displacements simultaneously from daily coordinates. The postseismic time series are likely not contaminated by the common mode error (Figures S2-S4), so we skipped the common mode error removal for the daily coordinates. The coseismic and postseismic displacements are inferred by fitting a function (Equation (1))

$$x(t) = a + \left(b + c\,\log\left(1 + \frac{t}{\tau}\right)\right)\mathrm{H}(t) \tag{1}$$

where, $x(t)$ is a position at time t with $t = 0$ being the mainshock date, $\mathrm{H}(t)$ is a Heaviside step function, and τ is a time constant (Figure 2a, c, and e). We determined a, b, and c by linear least square regression and τ by grid search. Here, we used the data ranging from one month before to one week after the mainshock date. We used one week of postseismic deformation to discuss the short-term dynamics of the afterslip at its earliest stage. We verified that one week of observation sufficiently captured the earliest decay of postseismic transient motion at most sites (Figures S2-S4), which is therefore sufficient to image the earliest afterslip process. We let each component at each site have a different τ because this trajectory model fit aims to extract coseismic and postseismic displacements from fluctuating time series. Therefore, we do not interpret the obtained τ values themselves. Then, we separated the postseismic displacement by subtracting the coseismic displacement derived from the 5-minute coordinates from the model prediction from Equation (1) (Figures 3a-b and S5). We estimated the errors for the coseismic displacements by combining the standard deviation of the pre-mainshock and post-mainshock position estimation (Figures S6a and S7a). For the postseismic displacement errors, we combined the standard deviation of residual daily time series and the coseismic displacement errors (Figures S6b and S7b). Although mostly within the standard deviation, both horizontal coseismic and postseismic displacements exhibit a systematic pattern pointing the mainshock epicenter, which is typical of megathrust earthquakes in subduction zones. The vertical error is much higher than the horizontal error and all the displacements are within the error level. Yet, the coseismic coastal subsidence and tiny inland displacements likely represent the mainshock signal taking place offshore. The postseismic vertical displacements also exhibit coastal subsidence, but the inland displacements have similar amplitude without a systematic pattern, meaning that most of the postseismic vertical displacements are likely noise.

For the following reasons, we combined the daily and 5-minute coordinates to derive coseismic and postseismic displacements. Typical analysis routine of daily coordinates uses all the observables from each day, meaning that the mainshock day position is derived from observables both before and after the mainshock; therefore, the mainshock day coordinate does not represent a position before or after the mainshock. This compels us to set the origin of postseismic deformation to the next day of the mainshock day which usually significantly underestimates the post-seismic displacement estimates (Twardzik et al., 2019). In our case, our coseismic displacements derived from the 5-min coordinates do not match with those measured using the daily coordinate on the mainshock day or the next day (Figure 2). Measuring postseismic displacements from the next day would decrease the postseismic displacement estimate by 25% at G088 for the east component (Figures 2a-b), which would impact the resultant afterslip amount.

2.2 Slip inversion

We inverted the obtained coseismic and postseismic displacements to infer coseismic slip and 1-week afterslip, respectively (Figure 3), using an inversion code SDM (L. Wang et al., 2009; R. Wang et al., 2013a). We discretized the three-dimensional curved slab interface (Iwasaki et al., 2015) into small rectangle subfaults and computed Green's functions in an isotropic homogeneous half-space (Okada, 1985). To stabilize the solution, we imposed a Laplacian smoothness constraint on the slip. Also, the rake angle was constrained to be between 30 and 150 degrees. For our preferred afterslip solution, we masked the subfaults with $\geq$ 1.4 m coseismic slip and forced their slip amplitude to be zero to assure that the substantial part of coseismic slip and afterslip do not overlap with each other (e.g., Itoh et al., 2019; Miyazaki et al., 2004; Scholz, 1998). All the data were weighted according to the observation error of the displacements. We chose a strength of the smoothness constraint based on a trade-off curve between misfits weighted by the displacement standard deviations and slip roughness (Figures S8 and S9) (L. Wang et al., 2009; R. Wang et al., 2013a). We did not use the vertical displacements for the preferred afterslip solution as their spatial pattern is highly unreliable (Figure S5b). Yet, we performed a test afterslip inversion with the vertical displacements and confirmed that main features of the inferred afterslip pattern did not dramatically change with or without them (Figures 3a-b and S10).

3 Results and discussion

3.1 Coseismic slip and afterslip

The estimated coseismic slip is located south of the rupture areas of the two 1996 earthquakes (Figure 3a), so the 2024 event is not a recurrence of ruptures of the slip patches hosting the 1996 events. This is consistent with the low slip deficit rate (e.g., T. Nishimura et al., 2018; Noda et al., 2018; Wallace et al., 2009) in terms of slip budget. The trade-off curve suggests that our preferred solution might be a little overfit (Figures S8a), but a smoother solution at the corner of the trade-off curve has a peak largely overlapping with the aftershocks, which is physically unreasonable (Figures S8b). The primary peak of the afterslip is located up-dip of the mainshock rupture area (Figure 3b), contrary to the down-dip afterslips following the two 1996 earthquakes (Figure 1a; Yagi et al., 2001). Without the mask of slip in the afterslip estimation, the substantial part of the afterslip overlaps with the coseismic slip area (Figure S11a). Such overlap is unlikely in terms of elementary behavior of frictional fault (e.g., Scholz, 1998) and most of the past observations in Hyuganada and elsewhere (e.g., Itoh et al., 2019; Miyazaki et al., 2004; Perfettini et al., 2010; Yagi et al., 2001). Hence, we found it more reasonable to choose the model masking the coseismic slip peak. The other afterslip patch is located in the down-dip extension of the mainshock at 30-40 km depths, which extends along-strike to the southwest away from the mainshock slip. The down-dip afterslip peak is located at its southernmost part, away from the mainshock patch. Interestingly, little afterslip was inferred in a small segment south of the mainshock and northeast of the down-dip afterslip peak (Figure 3b). To verify these features, we performed test afterslip inversions in which we masked a part of the fault plane in addition to the coseismic slip peak area (Figures S11b-d). We found that (1) masking the entire down-dip afterslip area did not increase afterslip in the little-afterslip segment south of the mainshock (Figures S11c) and (2) masking the southern part of the fault domain (Figures S11b and d) decreased the model prediction at the southern Kyushu, especially away from the coast (Figures S11c-d). Hence, we concluded that the down-dip afterslip peak to the southwest and the little amplitude of afterslip south of the mainshock rupture are not artifacts. On the other hand, the down-dip afterslip at the mainshock strike location is not reliable because its down-dip location is sensitive to whether we used the vertical displacements (Figures 3a-b and S10) and we gained fairly good horizontal fit without it (Figures S11c-d). The inferred moment magnitude of the preferred coseismic slip and afterslip models is M_w 7.0, and M_w 6.7, respectively, with a rigidity of 30 GPa.

3.2 Possible modulation of slip processes by the subducted seamount

The estimated coseismic slip and the primary peak of afterslip are located mostly within the broad estimate of the subducted KPR by Yamamoto et al. (2013) (Figures 3a-b). Inside this broad zone, the RTP magnetic anomaly suggests heterogeneous megathrust topography, and the estimated coseismic slip is located on the down-dip extension of the local seamount (Figure 3a) (Arai et al., 2023; Okino, 2015). We speculate that the coseismic slip propagation was impeded by the seamount acting as a soft barrier (K. Wang & Bilek, 2011), similar to an example of the 2008 Ibaraki-oki earthquake in the Japan Trench subduction zone (Kubo & Nishikawa, 2020). The occurrence of this mainshock in the low slip deficit rate area (Figures 3c-d; T. Nishimura et al., 2018; S. Nishimura & Hashimoto, 2006; Noda et al., 2018; Wallace et al., 2009) might pose a question to its occurrence mechanism considering the classical framework of backslip model (Savage, 1983). We speculate that there exist unresolved small fully locked patches in the mainshock zone and their rupture occurrence was assisted by the down-dip compression enhanced by the up-dip seamount (Sun et al., 2020).

The afterslip has a primary peak at the up-dip extension of the mainshock accompanied by the aftershock activity (Figures 3c-d and 4a). The radial aftershock front migration is well characterized as a logarithmic expansion with time as observed in many other cases (e.g., Frank et al., 2017; Kato & Obara, 2014; Peng & Zhao, 2009; Ross et al., 2017) (Figures 4b). The migration velocity is roughly at an order of 100 km/day at the very beginning and subsequently decreased roughly to an order of 10 km/day when reaching $\sim$50 km from the epicenter (Figure S12). Among these 1-week aftershocks, we visually identified four clusters of them, from AF1 to AF4 (Figure 4a). AF1 and AF2 are located next to the coseismic slip peak while AF3 and AF4 are located further up-dip, near the up-dip edge of the 1-week cumulative afterslip patch. Interestingly, the activation timing of cluster AF3 is similar to cluster AF4 although the epicentral distance of AF3 is $\sim$ 20 km shorter than AF4. Some small aftershocks might be missing in our JMA catalog right after large earthquakes (Figure S13a; e.g., Kagan, 2004), but the activation timing of AF3 and AF4 was still close only with larger magnitude aftershocks (Figures S13b-c).

This 1-week aftershock activity provides an interesting insight into the afterslip processes up-dip of the mainshock rupture (Figure 4a). Assuming that the aftershock migration front marks the migration front of afterslip (e.g., Kato & Obara, 2014; Peng & Zhao, 2009; Perfettini & Avouac, 2004; Perfettini et al., 2018), the activation of AF3 and AF4 at a similar timing means that the afterslip front migration toward AF3 is significantly slower than that toward AF4. This is seemingly consistent with a longer duration of aftershock activity of AF3 than AF4 (Figures 4b and S12a; Danré et al., 2024). Only cluster AF3 is located up-dip of the seamount, so we propose that the seamount impacted the up-dip migration speed of afterslip from AF1 and AF2 to AF3. In general, propagation speed of rupture/slip depends primarily on effective normal stress and shear stress and strength as shown by numerical simulations employing the rate-and-state friction law (e.g., Ariyoshi et al., 2019; Ozawa et al., 2023; Yang et al., 2012). Numerical simulations of afterslip demonstrate that afterslip migration speed is slower when effective normal stress on the interface is higher and so is the shear strength (Ariyoshi et al., 2019). As subducted seamounts produce higher effective normal stress from its top to the down-dip leading flank (Ruh et al., 2016; Sun et al., 2020), the effective normal stress along the migration path between AF1/AF2 and AF3 could be higher than that between AF2 and AF4, which is probably responsible for the slower afterslip front and aftershock migration. The low interseismic slip deficit rate at the seamount location (Figures 1a-b), perhaps due to the presence of fractured seamount (K. Wang & Bilek, 2011, 2014), implies a low level of accumulated shear stress on and around the seamount prior to the mainshock. This could also contribute to the decrease in migration speed of the afterslip front toward AF3. We cannot rule out the possibility that AF3 was activated by different processes such as a down-dip migration of shallow slip earthquakes which happened in 2010 (Uchida et al., 2020). Yet, we conclude that the possible contrast in afterslip migration observationally unveiled another hidden role of seamounts in modulating fault slip behavior. We did not perform time-dependent afterslip inversions because the dominant migration process finished around one day following the mainshock (Figure 4b) and the 5-minute GNSS coordinates would be too noisy to resolve temporal evolution of slip offshore considering the anticipated signal to noise ratio (Figure 2) (e.g., Itoh & Aoki, 2022; Twardzik et al., 2019).

This up-dip afterslip patch extends to the narrow area among the two 1996 and the 2024 mainshock rupture areas (Figure 3b), marked by the presence of clustered aftershocks AF1 (Figure 4a). These interlaced seismic and aseismic peaks illustrate the presence of mechanical heterogeneity at a 10 km scale, which is usually challenging to resolve for offshore megathrust. The presence of this upcoming afterslip area might have impeded the 2024 earthquake rupture (e.g., Itoh et al., 2023; Rolandone et al., 2018) and prevented it from entering the 1996 rupture areas. The peak of the down-dip afterslip patch away from the mainshock rupture was perhaps triggered by dynamic stress perturbation (Figure 3b), similar to some earlier examples (e.g., Itoh et al., 2023; Rolandone et al., 2018; Wallace et al., 2018).

3.3 Segment south of the mainshock area with little afterslip

The 1-week afterslip is little in the segment south of the mainshock rupture, where only a few aftershocks occurred during the first week (Figure 3b). This gap is located in the low interseismic slip deficit rate zone (Figures 3c-d; e.g., T. Nishimura et al., 2018). Moderate ordinary interplate earthquakes (M_w 4.1 to 5.5) between 2001 and 2019 (Takemura et al., 2020b) are absent in this gap, where most of the ordinary seismicity located near the interface between 2016 and the 2024 mainshock has a magnitude M_{JMA} below 2 (Figures 3c and S14), implying that seismic patches occupied very limited portion of moment release before the 2024 event. The repeating earthquake activity (Igarashi, 2020) and short- and long-term slow slip events (Okada et al., 2022; Ozawa et al., 2024; Takagi et al., 2016, 2019) (Figure 3d) are also scarce there, indicating a lack of transient acceleration of aseismic creep during the interseismic period. These observations imply that the interseismic aseismic creep in this segment was steady over time before the mainshock. Hence, the megathrust fault in this segment might continue to creep after the mainshock at a much slower rate than the afterslip peak, possibly close to the interseismic rate. The presence of such a very steady creep fault insusceptible to stress change probably requires high spatial variation in velocity strengthening frictional properties (Marone et al., 1991; Perfettini & Avouac, 2004; Scholz, 1998). The subducted KPR (Yamamoto et al., 2013) might be able to realize such short-wavelength (10 km order) heterogeneity of frictional parameters and stress state on the megathrust. As this apparent afterslip gap is not accompanied by a subducted seamount in its up-dip extension, the absence of seamount-induced enhanced down-dip compression (Ruh et al., 2016; Sun et al., 2020) might also assist such a creeping nature, in contrast to the mainshock segment.

4 Summary

The 2024 Hyuganada earthquake occurred along the creeping megathrust due to the presence of subducted KPR. We inferred the coseismic slip and 1-week afterslip of the 2024 Hyuganada earthquake using the observed displacements by GNSS. The comparison of the inferred slip models with the aftershocks, the ordinary earthquakes before the mainshocks, the slow earthquakes, and the local seamount, we illustrated the role of subducted seamounts in controlling coseismic and afterslip behavior (Figure 5). The mainshock occurred in the down-dip extension of the subducted seamount. Subducted seamounts enhance the compressional stress in its leading flank, developing favorable conditions for ordinary earthquake generation. Hence, the mainshock occurrence in the low interseismic slip deficit megathrust was probably assisted by the up-dip seamount (Figure 5a). During the coseismic stage (Figure 5b), the mainshock rupture likely extended toward the up-dip direction, which was arrested by the subducted seamount acting as a soft barrier. The northward rupture expansion was probably arrested by the megathrust which hosted the subsequent afterslip. Following the mainshock (Figure 5c), we identified two patches of the 1-week afterslip. The primary patch is located up-dip of the mainshock peak, which is accompanied by the four aftershock clusters. Based on the spatiotemporal aftershock activity, we proposed that the up-dip expansion of the afterslip front is slowed down while passing the seamount. With the series of afterslip inversion tests, we confirmed that little afterslip occurred in the small segment south of the mainshock, consistent with the scarce aftershock activity during the first week. Given the geodetically inferred interseismic creep and various tectonic slip phenomena before the 2024 event in this segment, we speculate that this segment is somehow insusceptible to external stress perturbation and continued to creep at a much lower rate than the afterslip peak following the mainshock. Our coseismic slip and afterslip overall illuminates heterogeneous mechanical properties at an order of $\sim$10 km, which is perhaps realized by the ridge subduction.

Open Research Section

The GNSS coordinates (Blewitt et al., 2018) are available as Nevada Geodetic Laboratory (2024). The plate model (Iwasaki et al., 2015) is available as Iwasaki (2024). Tectonic tremors (Yamashita et al., 2015, 2021) and repeaters (Igarashi, 2020) are available at Slow Earthquake Database Science of Slow Earthquakes (2024) developed by Kano et al. (2018). The slip model of Yagi et al. (1998) is available at Earthquake Source Model

Database (2024) in SRCMOD (Mai & Thingbaijam, 2014). The CMT solutions of Takemura et al. (2020b) are available at Takemura et al. (2020a). The JMA hypocenter catalog are available at Japan Meteorological Agency (2024a, 2024b). The slip inversion code SDM (L. Wang et al., 2009; R. Wang et al., 2013a) is available as R. Wang et al. (2013b). We will upload our products to Zenodo once the manuscript is accepted for publication. We provide their files in a zip file attached in the submission for peer review.

Acknowledgments

Discussions with Cedric Twardzik, Shunsuke Takemura, Yusuke Yamashita, So Ozawa, Saeko Kita, Yutaro Okada, Takashi Tonegawa, Ryo Okuwaki, Kelin Wang, Yosuke Aoki, Louise Maubant, Pierre Romanet, Yuqing Xie, Anne Socquet, and Romain Jolivet were fruitful. Yuji Yagi, Yutaro Okada, Ryuta Arai, and Takuya Nishimura kindly shared their products with us, which were published as Yagi et al. (1999, 2001), Okada et al. (2022), Arai et al. (2023), and T. Nishimura et al. (2018), respectively. The plate models by Iwasaki et al. (2015) were constructed from topography and bathymetry data by Geospatial Information Authority of Japan (250-m digital map), Japan Oceanographic Data Center (500m mesh bathemetry data, J-EGG500) and Geographic Information Network of Alaska, University of Alaska (Lindquist et al., 2004). The manuscript was improved by constructive comments from Andrew Newman and the two anonymous reviewers. This study is supported by Japan Society for the Promotion of Science (JSPS) KAKENHI JP21K14007 and JP21K03694 and by The University of Tokyo Excellent Young Researcher Project all awarded to YI.

References

Ando, M. (1975). Source mechanisms and tectonic significance of historical earthquakes along the nankai trough, japan. *Tectonophysics*, *27*(2), 119-140. Retrieved from `https://www.sciencedirect.com/science/article/pii/004019517590102X` doi: https://doi.org/10.1016/0040-1951(75)90102-X

Arai, R., Miura, S., Nakamura, Y., Fujie, G., Kodaira, S., Kaiho, Y., … others (2023). Upper-plate conduits linked to plate boundary that hosts slow earthquakes. *Nature Communications*, *14*(1), 5101. doi: https://doi.org/10.1038/s41467-023-40762-4

Ariyoshi, K., Ampuero, J.-P., Bürgmann, R., Matsuzawa, T., Hasegawa, A., Hino, R., & Hori, T. (2019). Quantitative relationship between aseismic slip propagation speed and frictional properties. *Tectonophysics*, *767*, 128151. Retrieved from `https://www.sciencedirect.com/science/article/pii/S0040195119302525` doi: https://doi.org/10.1016/j.tecto.2019.06.021

Blewitt, G., Hammond, W. C., & Kreemer, C. (2018). Harnessing the gps data explosion for interdisciplinary science. *EOS*, *99*. doi: 10.1029/2018EO104623

Choi, K., Bilich, A., Larson, K. M., & Axelrad, P. (2004). Modified sidereal filtering: Implications for high-rate gps positioning. *Geophysical Research Letters*, *31*(22). doi: 10.1029/2004GL021621

Danré, P., De Barros, L., Cappa, F., & Passarelli, L. (2024). Parallel dynamics of slow slips and fluid-induced seismic swarms. *Nature Communications*, *15*(1), 8943. doi: https://doi.org/10.1038/s41467-024-53285-3

DeMets, C., Gordon, R. G., & Argus, D. F. (2010, 04). Geologically current plate motions. *Geophysical Journal International*, *181*(1), 1-80. Retrieved from `https://doi.org/10.1111/j.1365-246X.2009.04491.x` doi: 10.1111/j.1365-246X.2009.04491.x

Earthquake Source Model Database. (2024). *s1968hyugax01yagi [dataset].* Retrieved from `http://equake-rc.info/SRCMOD/searchmodels/viewmodel/s1968HYUGAx01YAGI/`

Frank, W. B., Poli, P., & Perfettini, H. (2017). Mapping the rheology of the central chile subduction zone with aftershocks. *Geophysical Research Letters*, *44*(11), 5374-5382. Retrieved from https://agupubs.onlinelibrary.wiley.com/doi/abs/10.1002/2016GL072288 doi: https://doi.org/10.1002/2016GL072288

Igarashi, T. (2020). Catalog of small repeating earthquakes for the japanese islands. *Earth, Planets and Space*, *72*(1), 1–8. doi: https://doi.org/10.1186/s40623-020-01205-2

Ioki, K., Yamashita, Y., & Kase, Y. (2023). Effects of the tsunami generated by the 1662 hyuga-nada earthquake off miyazaki prefecture, japan. *Pure and Applied Geophysics*, *180*(6), 1897–1907. doi: https://doi.org/10.1007/s00024-022-03198-3

Itoh, Y., & Aoki, Y. (2022). On the performance of position-domain sidereal filter for 30-s kinematic gps to mitigate multipath errors. *Earth, Planets and Space*, *74*(1), 1–20. doi: 10.1186/s40623-022-01584-8

Itoh, Y., Nishimura, T., Ariyoshi, K., & Matsumoto, H. (2019). Interplate slip following the 2003 tokachi-oki earthquake from ocean bottom pressure gauge and land gnss data. *Journal of Geophysical Research: Solid Earth*, *124*(4), 4205-4230. Retrieved from https://agupubs.onlinelibrary.wiley.com/doi/abs/10.1029/2018JB016328 doi: https://doi.org/10.1029/2018JB016328

Itoh, Y., Socquet, A., & Radiguet, M. (2023). Largest aftershock nucleation driven by afterslip during the 2014 iquique sequence. *Geophysical Research Letters*, *50*(24), e2023GL104852. Retrieved from https://agupubs.onlinelibrary.wiley.com/doi/abs/10.1029/2023GL104852 (e2023GL104852 2023GL104852) doi: https://doi.org/10.1029/2023GL104852

Iwasaki, T. (2024). *Plate boundary models in and around japan [dataset].* Retrieved from http://evrrss.eri.u-tokyo.ac.jp/database/PLATEmodel/PLMDL_2016/

Iwasaki, T., Sato, H., Ishiyama, T., Shinohara, M., & Hashima, A. (2015, December). Fundamental structure model of island arcs and subducted plates in and around Japan. In *Agu fall meeting abstracts* (Vol. 2015, p. T31B-2878).

Japan Meteorological Agency. (2024a). *[dataset].* Retrieved from https://www.data.jma.go.jp/svd/eqev/data/bulletin/hypo_e.html

Japan Meteorological Agency. (2024b). *[dataset].* Retrieved from https://www.data.jma.go.jp/eqev/data/daily_map/index.html

Kagan, Y. Y. (2004, 08). Short-term properties of earthquake catalogs and models of earthquake source. *Bulletin of the Seismological Society of America*, *94*(4), 1207-1228. Retrieved from https://doi.org/10.1785/012003098 doi: 10.1785/012003098

Kano, M., Aso, N., Matsuzawa, T., Ide, S., Annoura, S., Arai, R., ... others (2018). Development of a slow earthquake database. *Seismological Research Letters*, *89*(4), 1566–1575. doi: https://doi.org/10.1785/0220180021

Kato, A., & Obara, K. (2014). Step-like migration of early aftershocks following the 2007 m 6.7 noto-hanto earthquake, japan. *Geophysical Research Letters*, *41*(11), 3864-3869. Retrieved from https://agupubs.onlinelibrary.wiley.com/doi/abs/10.1002/2014GL060427 doi: https://doi.org/10.1002/2014GL060427

Kubo, H., & Nishikawa, T. (2020). Relationship of preseismic, coseismic, and postseismic fault ruptures of two large interplate aftershocks of the 2011 tohoku earthquake with slow-earthquake activity. *Scientific reports*, *10*(1), 12044. doi: https://doi.org/10.1038/s41598-020-68692-x

Lindquist, K. G., Engle, K., Stahlke, D., & Price, E. (2004). Global topography and bathymetry grid improves research efforts. *Eos, Transactions American Geophysical Union*, *85*(19), 186-186. Retrieved from https://agupubs.onlinelibrary.wiley.com/doi/abs/10.1029/2004EO190003 doi: https://doi.org/10.1029/2004EO190003

Mai, P. M., & Thingbaijam, K. K. S. (2014, 10). SRCMOD: An Online Database of Finite-Fault Rupture Models. *Seismological Research Letters*, *85*(6), 1348-1357. Retrieved from `https://doi.org/10.1785/0220140077` doi: 10.1785/0220140077

Marone, C. J., Scholtz, C. H., & Bilham, R. (1991). On the mechanics of earthquake afterslip. *Journal of Geophysical Research: Solid Earth*, *96*(B5), 8441-8452. Retrieved from `https://agupubs.onlinelibrary.wiley.com/doi/abs/10.1029/91JB00275` doi: https://doi.org/10.1029/91JB00275

Miyazaki, S., Segall, P., Fukuda, J., & Kato, T. (2004). Space time distribution of afterslip following the 2003 tokachi-oki earthquake: Implications for variations in fault zone frictional properties. *Geophysical Research Letters*, *31*(6). Retrieved from `https://agupubs.onlinelibrary.wiley.com/doi/abs/10.1029/2003GL019410` doi: https://doi.org/10.1029/2003GL019410

Mochizuki, K., Yamada, T., Shinohara, M., Yamanaka, Y., & Kanazawa, T. (2008). Weak interplate coupling by seamounts and repeating $M \sim 7$ earthquakes. *Science*, *321*(5893), 1194-1197. Retrieved from `https://www.science.org/doi/abs/10.1126/science.1160250` doi: 10.1126/science.1160250

Nevada Geodetic Laboratory. (2024). *[dataset].* Retrieved from `http://geodesy.unr.edu/`

Nishimura, S., & Hashimoto, M. (2006). A model with rigid rotations and slip deficits for the gps-derived velocity field in southwest japan. *Tectonophysics*, *421*(3), 187-207. Retrieved from `https://www.sciencedirect.com/science/article/pii/S0040195106002368` doi: https://doi.org/10.1016/j.tecto.2006.04.017

Nishimura, T., Yokota, Y., Tadokoro, K., & Ochi, T. (2018, 02). Strain partitioning and interplate coupling along the northern margin of the Philippine Sea plate, estimated from Global Navigation Satellite System and Global Positioning System-Acoustic data. *Geosphere*, *14*(2), 535-551. Retrieved from `https://doi.org/10.1130/GES01529.1` doi: 10.1130/GES01529.1

Noda, A., Saito, T., & Fukuyama, E. (2018). Slip-deficit rate distribution along the nankai trough, southwest japan, with elastic lithosphere and viscoelastic asthenosphere. *Journal of Geophysical Research: Solid Earth*, *123*(9), 8125-8142. Retrieved from `https://agupubs.onlinelibrary.wiley.com/doi/abs/10.1029/2018JB015515` doi: https://doi.org/10.1029/2018JB015515

Okada, Y. (1985, 08). Surface deformation due to shear and tensile faults in a half-space. *Bulletin of the Seismological Society of America*, *75*(4), 1135-1154. Retrieved from `https://doi.org/10.1785/BSSA0750041135` doi: 10.1785/BSSA0750041135

Okada, Y., Nishimura, T., Tabei, T., Matsushima, T., & Hirose, H. (2022). Development of a detection method for short-term slow slip events using gnss data and its application to the nankai subduction zone. *Earth, Planets and Space*, *74*(1), 1–18.

Okazaki, T., Fukahata, Y., & Nishimura, T. (2021). Consistent estimation of strain-rate fields from gnss velocity data using basis function expansion with abic. *Earth, Planets and Space*, *73*, 1–22. doi: https://doi.org/10.1186/s40623-021-01474-5

Okino, K. (2015). Magnetic anomalies in the philippine sea: Implications for regional tectonics. *Journal of Geography (Chigaku Zasshi)*, *124*(5), 729-747. doi: 10.5026/jgeography.124.729

Ozawa, S., Ando, R., & Dunham, E. M. (2023). Quantifying the probability of rupture arrest at restraining and releasing bends using earthquake sequence simulations. *Earth and Planetary Science Letters*, *617*, 118276. Retrieved from `https://www.sciencedirect.com/science/article/pii/S0012821X23002893` doi: https://doi.org/10.1016/j.epsl.2023.118276

Ozawa, S., Muneakane, H., & Suito, H. (2024). Time-dependent modeling of slow-slip events along the nankai trough subduction zone, japan, within the 2018–2023 period. *Earth, Planets and Space*, *76*(1), 23. doi: https://doi.org/10.1186/s40623-024-01970-4

Peng, Z., & Zhao, P. (2009). Migration of early aftershocks following the 2004 parkfield earthquake. *Nature Geoscience*, *2*(12), 877–881. doi: https://doi.org/10.1038/ngeo697

Perfettini, H., & Avouac, J.-P. (2004). Postseismic relaxation driven by brittle creep: A possible mechanism to reconcile geodetic measurements and the decay rate of aftershocks, application to the chi-chi earthquake, taiwan. *Journal of Geophysical Research: Solid Earth*, *109*(B2). Retrieved from `https://agupubs.onlinelibrary.wiley.com/doi/abs/10.1029/2003JB002488` doi: https://doi.org/10.1029/2003JB002488

Perfettini, H., Avouac, J.-P., Tavera, H., Kositsky, A., Nocquet, J.-M., Bondoux, F., . . . others (2010). Seismic and aseismic slip on the central peru megathrust. *Nature*, *465*(7294), 78–81. doi: https://doi.org/10.1038/nature09062

Perfettini, H., Frank, W. B., Marsan, D., & Bouchon, M. (2018). A model of aftershock migration driven by afterslip. *Geophysical Research Letters*, *45*(5), 2283-2293. Retrieved from `https://agupubs.onlinelibrary.wiley.com/doi/abs/10.1002/2017GL076287` doi: https://doi.org/10.1002/2017GL076287

Ragheb, A., Clarke, P. J., & Edwards, S. (2007). Gps sidereal filtering: coordinate- and carrier-phase-level strategies. *Journal of Geodesy*, *81*(5), 325–335. doi: 10.1007/s00190-006-0113-1

Rolandone, F., Nocquet, J.-M., Mothes, P. A., Jarrin, P., Vallée, M., Cubas, N., . . . Font, Y. (2018). Areas prone to slow slip events impede earthquake rupture propagation and promote afterslip. *Science Advances*, *4*(1), eaao6596. Retrieved from `https://www.science.org/doi/abs/10.1126/sciadv.aao6596` doi: 10.1126/sciadv.aao6596

Ross, Z. E., Rollins, C., Cochran, E. S., Hauksson, E., Avouac, J.-P., & Ben-Zion, Y. (2017). Aftershocks driven by afterslip and fluid pressure sweeping through a fault-fracture mesh. *Geophysical Research Letters*, *44*(16), 8260-8267. Retrieved from `https://agupubs.onlinelibrary.wiley.com/doi/abs/10.1002/2017GL074634` doi: https://doi.org/10.1002/2017GL074634

Ruh, J. B., Sallarès, V., Ranero, C. R., & Gerya, T. (2016). Crustal deformation dynamics and stress evolution during seamount subduction: High-resolution 3-d numerical modeling. *Journal of Geophysical Research: Solid Earth*, *121*(9), 6880-6902. Retrieved from `https://agupubs.onlinelibrary.wiley.com/doi/abs/10.1002/2016JB013250` doi: https://doi.org/10.1002/2016JB013250

Sagiya, T. (2004). A decade of geonet: 1994-2003. *Earth, Planets and Space*, *56*(8), xxix-xli. doi: 10.1186/BF03353077

Sagiya, T., Miyazaki, S., & Tada, T. (2000). Continuous gps array and present-day crustal deformation of japan. *Pure and applied Geophysics*, *157*, 2303–2322. doi: https://doi.org/10.1007/PL00022507

Sagiya, T., & Thatcher, W. (1999). Coseismic slip resolution along a plate boundary megathrust: The nankai trough, southwest japan. *Journal of Geophysical Research: Solid Earth*, *104*(B1), 1111-1129. Retrieved from `https://agupubs.onlinelibrary.wiley.com/doi/abs/10.1029/98JB02644` doi: https://doi.org/10.1029/98JB02644

Savage, J. C. (1983). A dislocation model of strain accumulation and release at a subduction zone. *Journal of Geophysical Research: Solid Earth*, *88*(B6), 4984-4996. Retrieved from `https://agupubs.onlinelibrary.wiley.com/doi/abs/10.1029/JB088iB06p04984` doi: https://doi.org/10.1029/JB088iB06p04984

Scholz, C. H. (1998). Earthquakes and friction laws. *Nature*, *391*(6662), 37–42. doi: https://doi.org/10.1038/34097

Science of Slow Earthquakes. (2024). *Slow earthquake database [dataset].* Retrieved from http://www-solid.eps.s.u-tokyo.ac.jp/~sloweq/

Smith, W. H. F., & Sandwell, D. T. (1997). Global sea floor topography from satellite altimetry and ship depth soundings. *Science*, *277*(5334), 1956-1962. Retrieved from https://www.science.org/doi/abs/10.1126/science.277.5334.1956 doi: 10.1126/science.277.5334.1956

Sun, T., Saffer, D., & Ellis, S. (2020). Mechanical and hydrological effects of seamount subduction on megathrust stress and slip. *Nature Geoscience*, *13*(3), 249–255. doi: https://doi.org/10.1038/s41561-020-0542-0

Takagi, R., Obara, K., & Maeda, T. (2016). Slow slip event within a gap between tremor and locked zones in the nankai subduction zone. *Geophysical Research Letters*, *43*(3), 1066-1074. Retrieved from https://agupubs.onlinelibrary.wiley.com/doi/abs/10.1002/2015GL066987 doi: https://doi.org/10.1002/2015GL066987

Takagi, R., Uchida, N., & Obara, K. (2019). Along-strike variation and migration of long-term slow slip events in the western nankai subduction zone, japan. *Journal of Geophysical Research: Solid Earth*, *124*(4), 3853-3880. Retrieved from https://agupubs.onlinelibrary.wiley.com/doi/abs/10.1029/2018JB016738 doi: https://doi.org/10.1029/2018JB016738

Takemura, S., Okuwaki, R., Kubota, T., Shiomi, K., Kimura, T., & Noda, A. (2020a, February). *3D CMT catalogue of moderate size offshore earthquakes along the Nankai Trough [Dataset].* Zenodo. Retrieved from https://doi.org/10.5281/zenodo.3674161 doi: 10.5281/zenodo.3674161

Takemura, S., Okuwaki, R., Kubota, T., Shiomi, K., Kimura, T., & Noda, A. (2020b, 05). Centroid moment tensor inversions of offshore earthquakes using a three-dimensional velocity structure model: slip distributions on the plate boundary along the Nankai Trough. *Geophysical Journal International*, *222*(2), 1109-1125. Retrieved from https://doi.org/10.1093/gji/ggaa238 doi: 10.1093/gji/ggaa238

Twardzik, C., Vergnolle, M., Sladen, A., & Avallone, A. (2019). Unravelling the contribution of early postseismic deformation using sub-daily gnss positioning. *Scientific reports*, *9*(1), 1775. doi: https://doi.org/10.1038/s41598-019-39038-z

Uchida, N., Takagi, R., Asano, Y., & Obara, K. (2020). Migration of shallow and deep slow earthquakes toward the locked segment of the nankai megathrust. *Earth and Planetary Science Letters*, *531*, 115986. Retrieved from https://www.sciencedirect.com/science/article/pii/S0012821X19306788 doi: https://doi.org/10.1016/j.epsl.2019.115986

Wallace, L. M., Ellis, S., Miyao, K., Miura, S., Beavan, J., & Goto, J. (2009, 02). Enigmatic, highly active left-lateral shear zone in southwest Japan explained by aseismic ridge collision. *Geology*, *37*(2), 143-146. Retrieved from https://doi.org/10.1130/G25221A.1 doi: 10.1130/G25221A.1

Wallace, L. M., Hreinsdóttir, S., Ellis, S., Hamling, I., D'Anastasio, E., & Denys, P. (2018). Triggered slow slip and afterslip on the southern hikurangi subduction zone following the kaikōura earthquake. *Geophysical Research Letters*, *45*(10), 4710-4718. Retrieved from https://agupubs.onlinelibrary.wiley.com/doi/abs/10.1002/2018GL077385 doi: https://doi.org/10.1002/2018GL077385

Wang, K., & Bilek, S. L. (2011, 09). Do subducting seamounts generate or stop large earthquakes? *Geology*, *39*(9), 819-822. Retrieved from https://doi.org/10.1130/G31856.1 doi: 10.1130/G31856.1

Wang, K., & Bilek, S. L. (2014). Invited review paper: Fault creep caused by subduction of rough seafloor relief. *Tectonophysics*, *610*, 1-24. Retrieved from https://www.sciencedirect.com/science/article/pii/S0040195113006896 doi: https://doi.org/10.1016/j.tecto.2013.11.024

Wang, L., Wang, R., Roth, F., Enescu, B., Hainzl, S., & Ergintav, S. (2009, 09).

Afterslip and viscoelastic relaxation following the 1999 M 7.4 İzmit earthquake from GPS measurements. *Geophysical Journal International*, *178*(3), 1220-1237. Retrieved from https://doi.org/10.1111/j.1365-246X.2009.04228.x doi: 10.1111/j.1365-246X.2009.04228.x

Wang, R., Diao, F., & Hoechner, A. (2013a). Sdm-a geodetic inversion code incorporating with layered crust structure and curved fault geometry. In *Egu general assembly conference abstracts* (pp. EGU2013–2411).

Wang, R., Diao, F., & Hoechner, A. (2013b). Sdm – a geodetic inversion code incorporating with layered crust structure and curved fault geometry. *GFZ [Software]*. Retrieved from https://www.gfz-potsdam.de/pub/home/turk/wang/ doi: https://gfzpublic.gfz-potsdam.de/pubman/item/item_1975902

Wdowinski, S., Bock, Y., Zhang, J., Fang, P., & Genrich, J. (1997). Southern california permanent gps geodetic array: Spatial filtering of daily positions for estimating coseismic and postseismic displacements induced by the 1992 landers earthquake. *Journal of Geophysical Research: Solid Earth*, *102*(B8), 18057-18070. doi: 10.1029/97JB01378

Yagi, Y., Kikuchi, M., & Sagiya, T. (2001). Co-seismic slip, post-seismic slip, and aftershocks associated with two large earthquakes in 1996 in hyuga-nada, japan. *Earth, planets and space*, *53*(8), 793–803. doi: https://doi.org/10.1186/BF03351677

Yagi, Y., Kikuchi, M., Yoshida, S., & Sagiya, T. (1999). Comparison of the coseismic rupture with the aftershock distribution in the hyuga-nada earthquakes of 1996. *Geophysical Research Letters*, *26*(20), 3161-3164. Retrieved from https://agupubs.onlinelibrary.wiley.com/doi/abs/10.1029/1999GL005340 doi: https://doi.org/10.1029/1999GL005340

Yagi, Y., Kikuchi, M., Yoshida, S., & Yamanaka, Y. (1998). Source process of the hyuga-nada earthquake of april 1, 1968 (m_{JMA}7.5), and its relationship to the subsequent seismicity. *Zisin (Journal of the Seismological Society of Japan. 2nd ser.)*, *51*(1), 139-148. doi: 10.4294/zisin1948.51.1_139

Yamamoto, Y., Obana, K., Takahashi, T., Nakanishi, A., Kodaira, S., & Kaneda, Y. (2013). Imaging of the subducted kyushu-palau ridge in the hyuga-nada region, western nankai trough subduction zone. *Tectonophysics*, *589*, 90-102. Retrieved from https://www.sciencedirect.com/science/article/pii/S0040195113000103 doi: https://doi.org/10.1016/j.tecto.2012.12.028

Yamashita, Y., Shinohara, M., & Yamada, T. (2021). Shallow tectonic tremor activities in hyuga-nada, nankai subduction zone, based on long-term broadband ocean bottom seismic observations. *Earth, Planets and Space*, *73*, 1–11. doi: https://doi.org/10.1186/s40623-021-01533-x

Yamashita, Y., Yakiwara, H., Asano, Y., Shimizu, H., Uchida, K., Hirano, S., ... Obara, K. (2015). Migrating tremor off southern kyushu as evidence for slow slip of a shallow subduction interface. *Science*, *348*(6235), 676-679. Retrieved from https://www.science.org/doi/abs/10.1126/science.aaa4242 doi: 10.1126/science.aaa4242

Yang, H., Liu, Y., & Lin, J. (2012). Effects of subducted seamounts on megathrust earthquake nucleation and rupture propagation. *Geophysical Research Letters*, *39*(24). Retrieved from https://agupubs.onlinelibrary.wiley.com/doi/abs/10.1029/2012GL053892 doi: https://doi.org/10.1029/2012GL053892

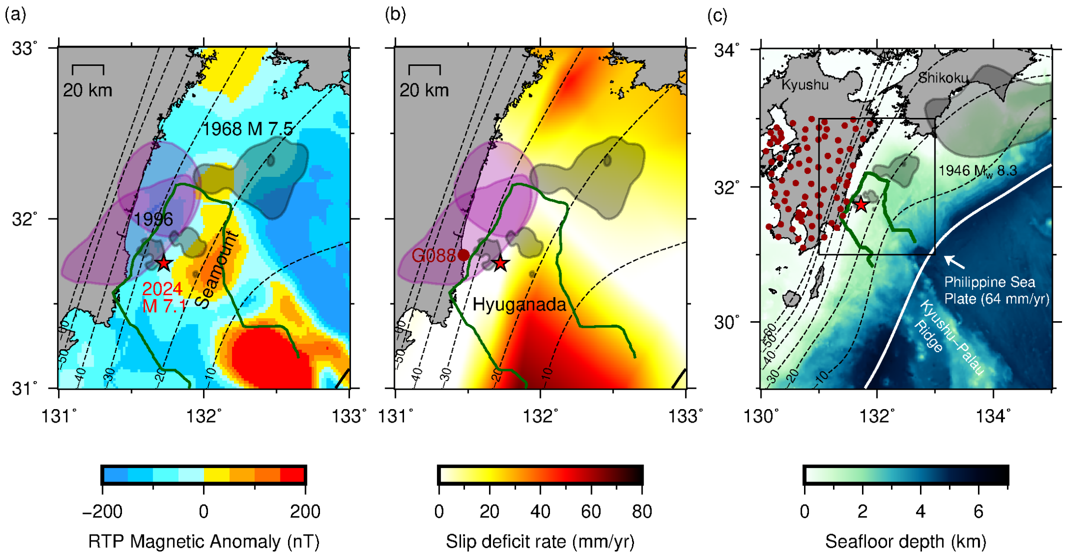

Figure 1. Tectonic setting. (a) The red star indicates the epicenter of the 2024 Hyuganada earthquake determined by the Japan Meteorological Agency. The half-transparent black shapes indicate outlines of the coseismic slip of the 1968 (1.2 m) and the two 1996 (0.5 m for both; M_w 6.8 and 6.7 for the October (shallow) and the December (deep) events, respectively) Hyuganada earthquakes (Yagi et al., 1998, 1999). Outlines of 4 cm slip of two afterslip models following the two 1996 earthquakes are drawn in purple (Yagi et al., 2001). The broken contours indicate slab surface depth (Iwasaki et al., 2015). The background color in the sea area is RTP magnetic anomaly (Arai et al., 2023; Okino, 2015). The dark green curve indicates the estimate of the spatial range of the subducted KPR inferred from a low seismic velocity belt (Yamamoto et al., 2013). (b) The background color indicates interseismic slip deficit rate between 2005 and 2009 (T. Nishimura et al., 2018). The brown dot indicates the location of an example GNSS site, G088, shown in Figure 2. (c) Broader map. Brown dots indicate all the GNSS sites used to infer the slip distributions (See Figure S1 for site codes). The half-transparent black shape outlines a 2 m slip area of the 1946 M_w 8.3 Nankaido earthquake (Sagiya & Thatcher, 1999). The vector seaward of the trench is a motion direction of the Philippine Sea Plate motion with respect to the Amur plate (DeMets et al., 2010). The seafloor depth in the background is after Smith and Sandwell (1997).

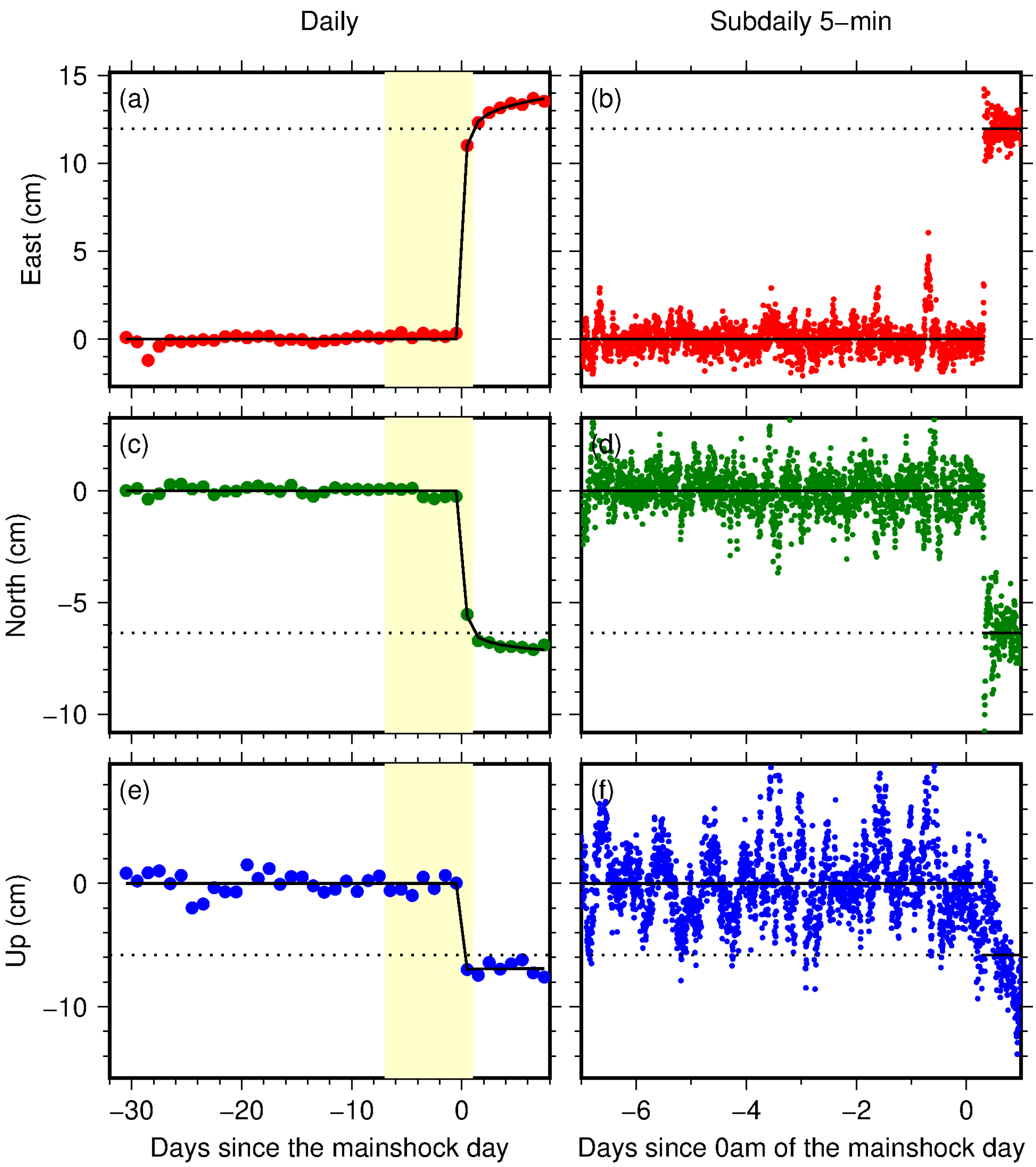

Figure 2. An example of GNSS time series at site G088 (Figure 1a). (a) East component of daily time series (red) with a function fit to it (black) using Equation (1). The dotted line is an immediate post-mainshock position inferred from 5-minute coordinates in (b). (b) East component of 5-minute time series (red) with the averaged pre- and post-mainshock positions (black). (c-f) Same as (a-b) but for north (c-d) and vertical (e-f) components. The typical noise level of each daily coordinate is ∼1 and ∼3 mm for horizontal and vertical components, respectively. The typical noise level of each subdaily coordinate is ∼7 mm and ∼3 cm for horizontal and vertical components, respectively.

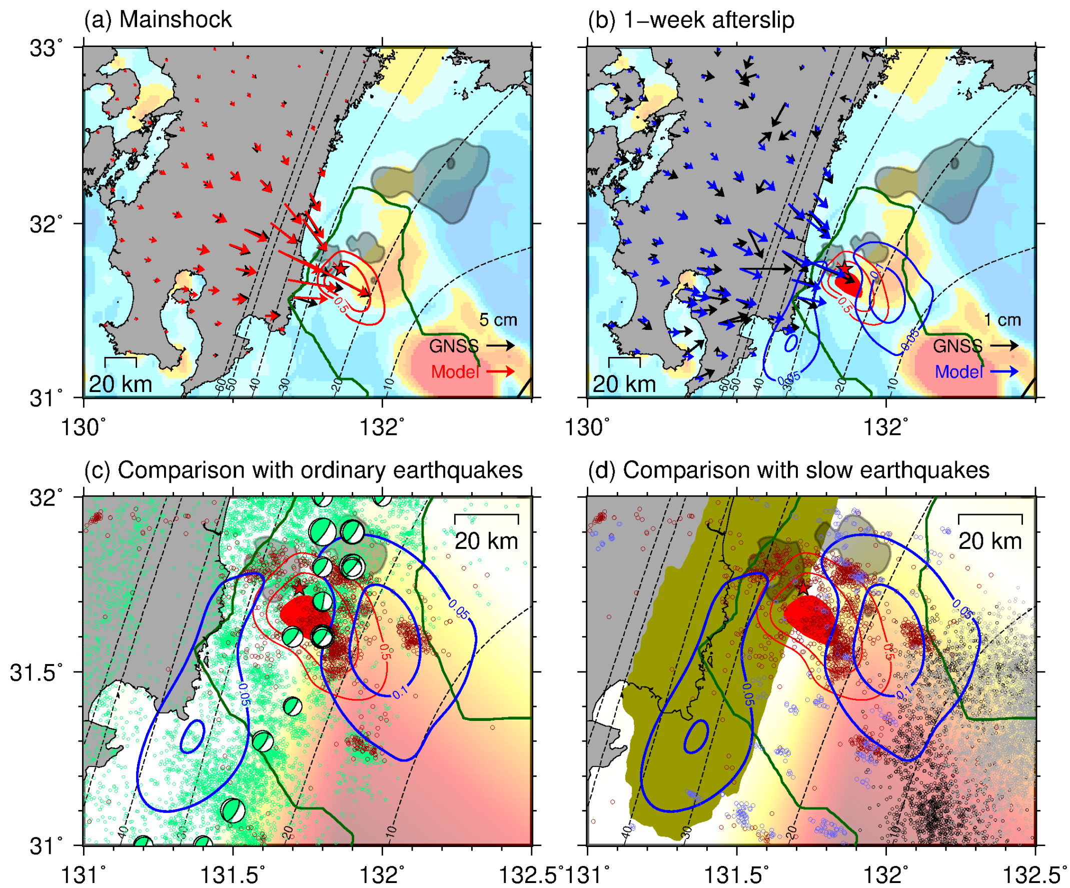

Figure 3. Inversion results. (a-b) Contours indicate the estimated coseismic (a, red) and 1-week afterslip (b, blue). The vectors indicate horizontal coseismic (a) and 1-week postseismic (b) displacements (black) with model predictions from the coseismic slip (a) and afterslip (b, blue). Vertical displacements are shown in Figure S5. We trimmed out error ellipses of the displacements for visual clarity and showed the displacements with the error ellipses in Figures S6. Typical nominal errors for these displacements are 1-2 cm. The brown open dots indicate 1-week aftershocks reported by JMA. In (b), the area with the coseismic slip $\geq$ 1.4 m is filled in red. (c-d) Comparison of the estimated coseismic slip and afterslip with various tectonic slip phenomena. (c) The green open dots indicate ordinary seismicity from April 1, 2016, to August 7, 2024, as reported by JMA. The beachballs indicate Centroid Moment Tensor (CMT) solutions of moderate earthquakes ranging between M_w 4.1 and 5.5 from 2004 to 2019 (Takemura et al., 2020b). (d) Blue open dots indicate repeating earthquakes from 1982 to 2019 (Igarashi, 2020). The area with more than 5 short-term SSEs from 1997 to 2020 is drawn in olive (Okada et al., 2022). The black and grey open dots tectonic tremors in 2013 and 2014-2017, respectively (Yamashita et al., 2015, 2021).Refer to Figure 1 for other elements.

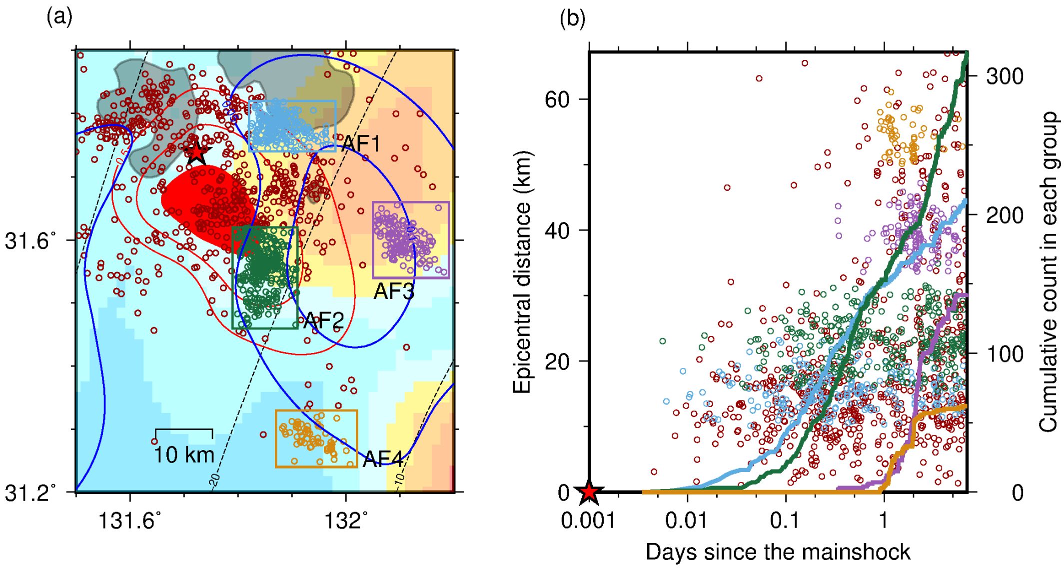

Figure 4. Seismicity analysis results. (a) Zoom-in plot of the coseismic slip and afterslip area. The two 1968 rupture areas are drawn in black. The selected four aftershock clusters are drawn with different colors as labeled. (b) Temporal evolution of seismicity in the radial direction from the epicenter. The star indicates the mainshock location and approximated timing. Refer to (a) for different colors. The curves indicate cumulative event counts measured every 5 minutes in each cluster with the corresponding colors. Refer to Figure 1 for other elements.

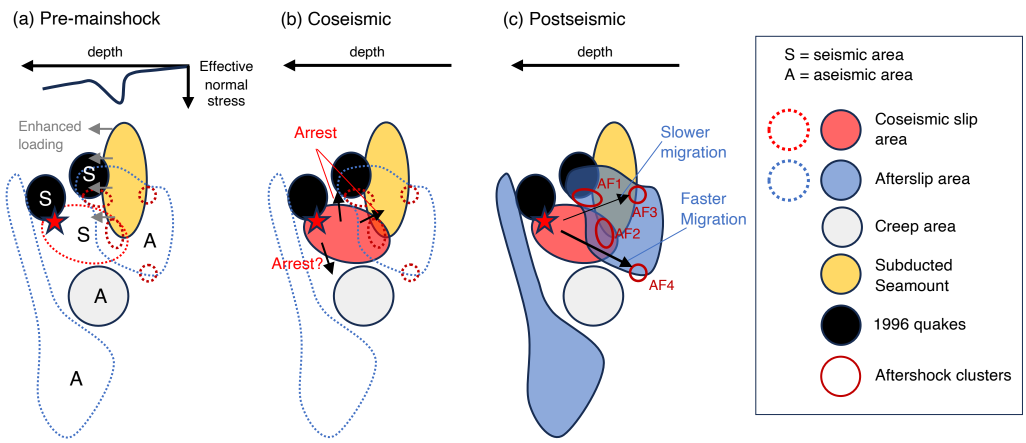

Figure 5. Schetch of the proposed occurrence scenario of the 2024 Hyuganada mainshock and afterslip. A schematic depth variation of effective normal stress associated with seamount subduction in (a) is hand-drawn after Sun et al. (2020).

Supporting Information for "Coseismic slip and early afterslip of the 2024 Hyuganada earthquake modulated by a subducted seamount"

Yuji Itoh[1]

[1]Earthquake Research Institute, The University of Tokyo, Japan

This is a non-peer-reviewed manuscript uploaded at EarthArXiv

Contents of this file

1. Figures S1 to S14

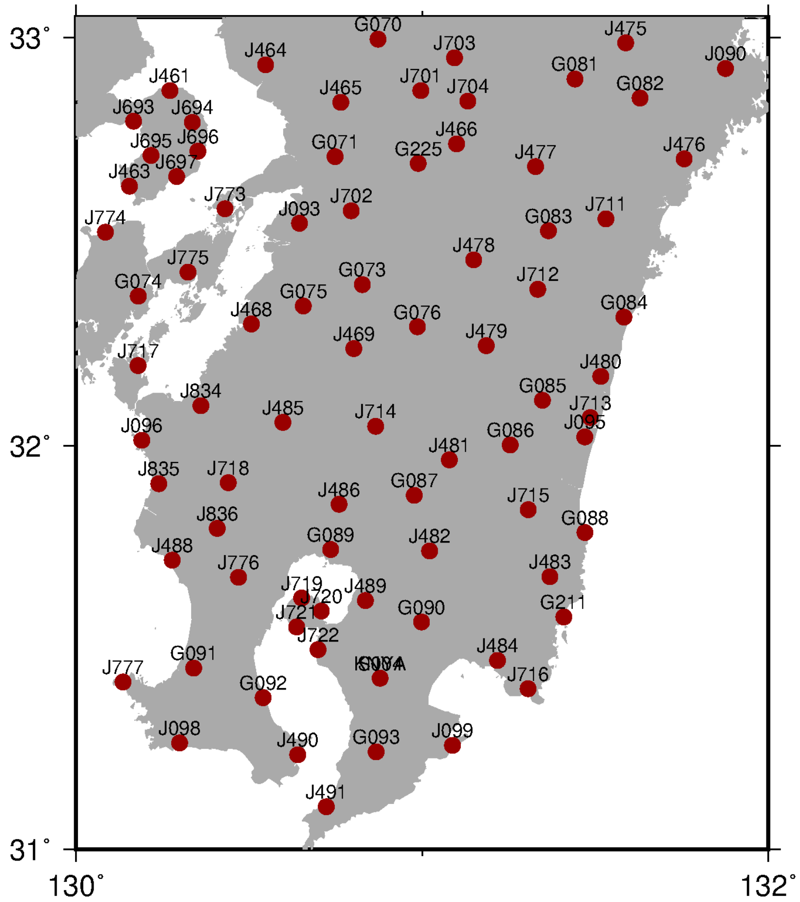

Figure S1. GNSS sites used in this study as labeled.

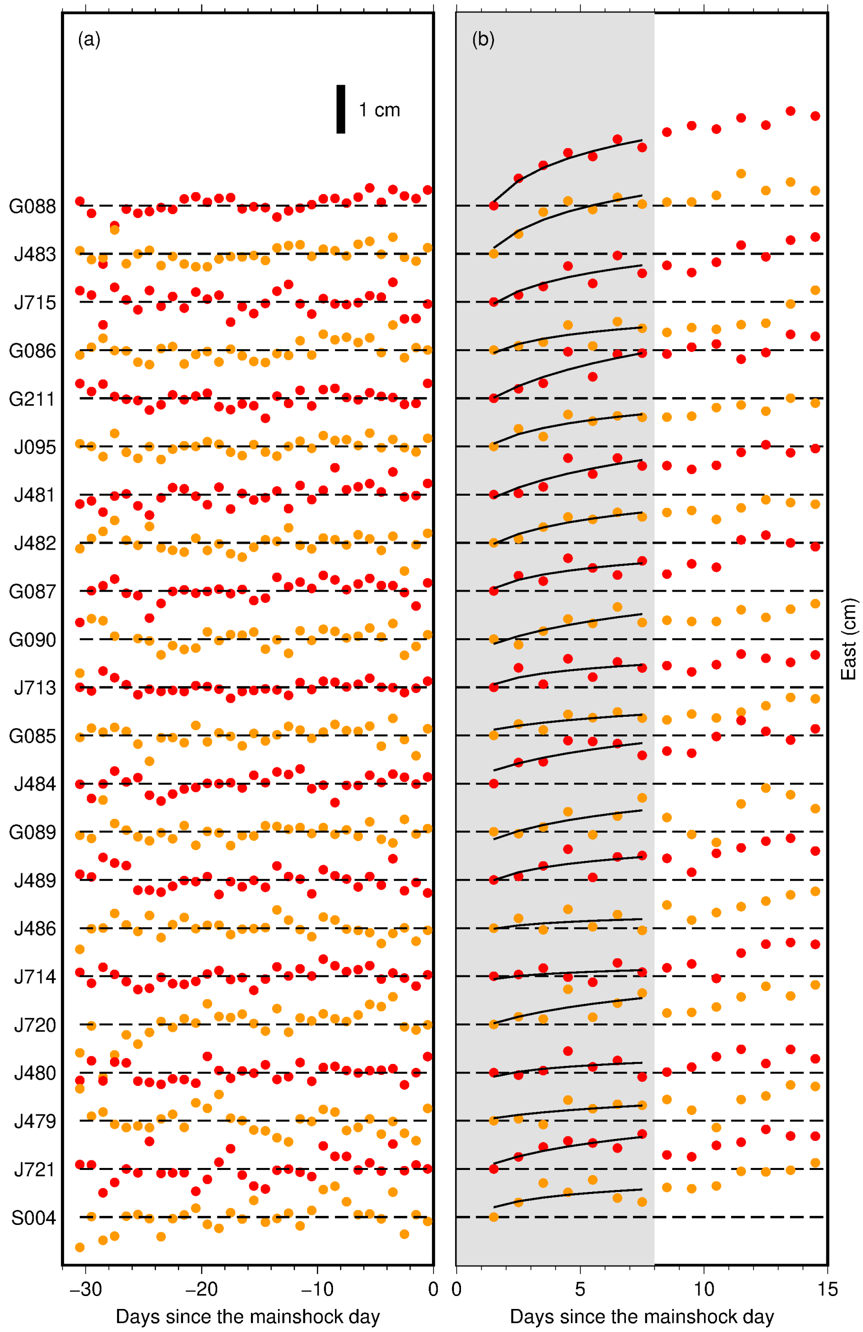

Figure S2. East component of daily GNSS time series (dots) at selected sites before (a) and after (b) the mainshock. (a) The pre-mainshock location is shown with broken lines. (b) The logarithmic fit (Equation (1)) and the position on the next day of the mainshock day are shown with solid curves and broken lines, respectively. The step on the mainshock day is removed between the two panels. We removed the data of the mainshock day from (b) because they do not represent a proper position before or after the mainshock. See the site location for Figure S1.

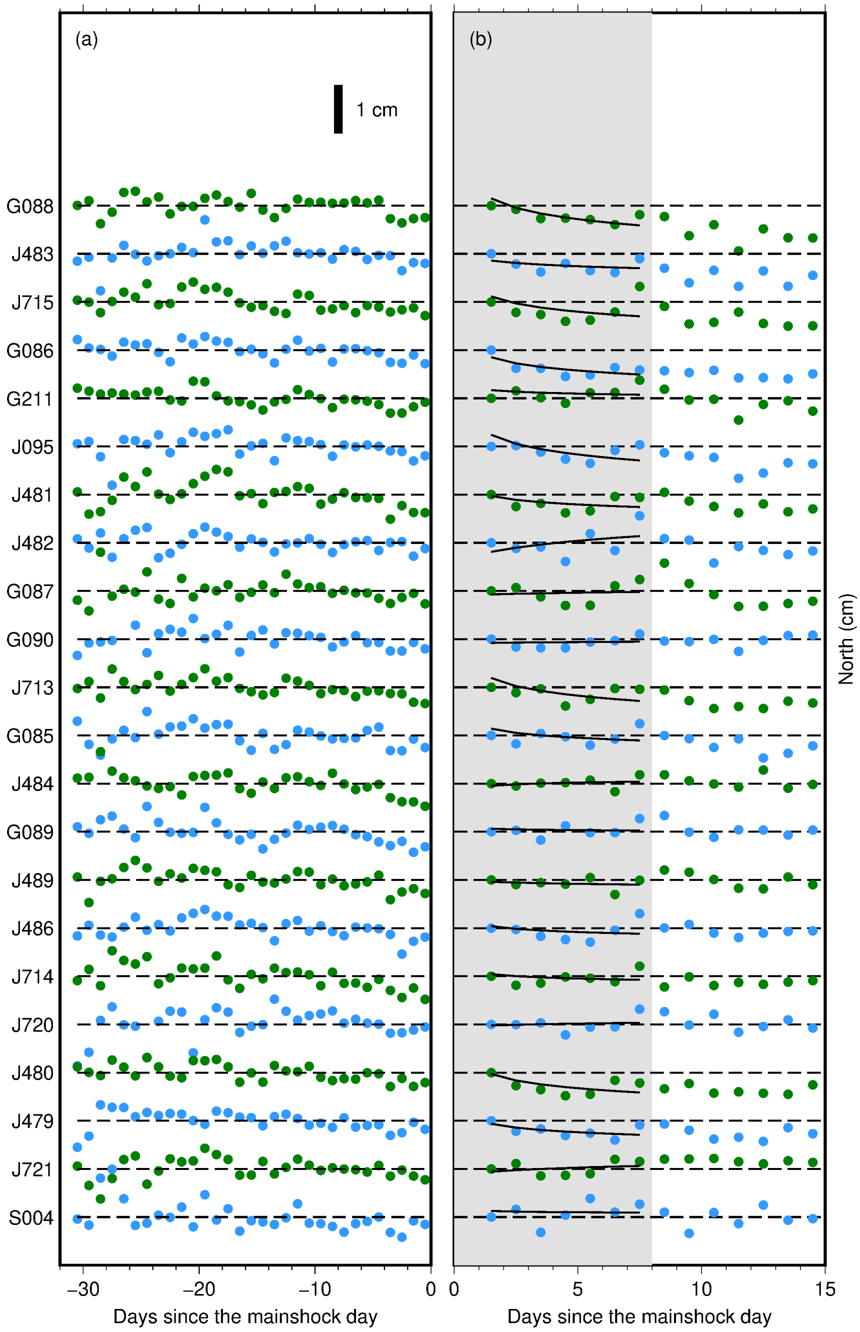

Figure S3. Same as Figure S2 but for the north component.

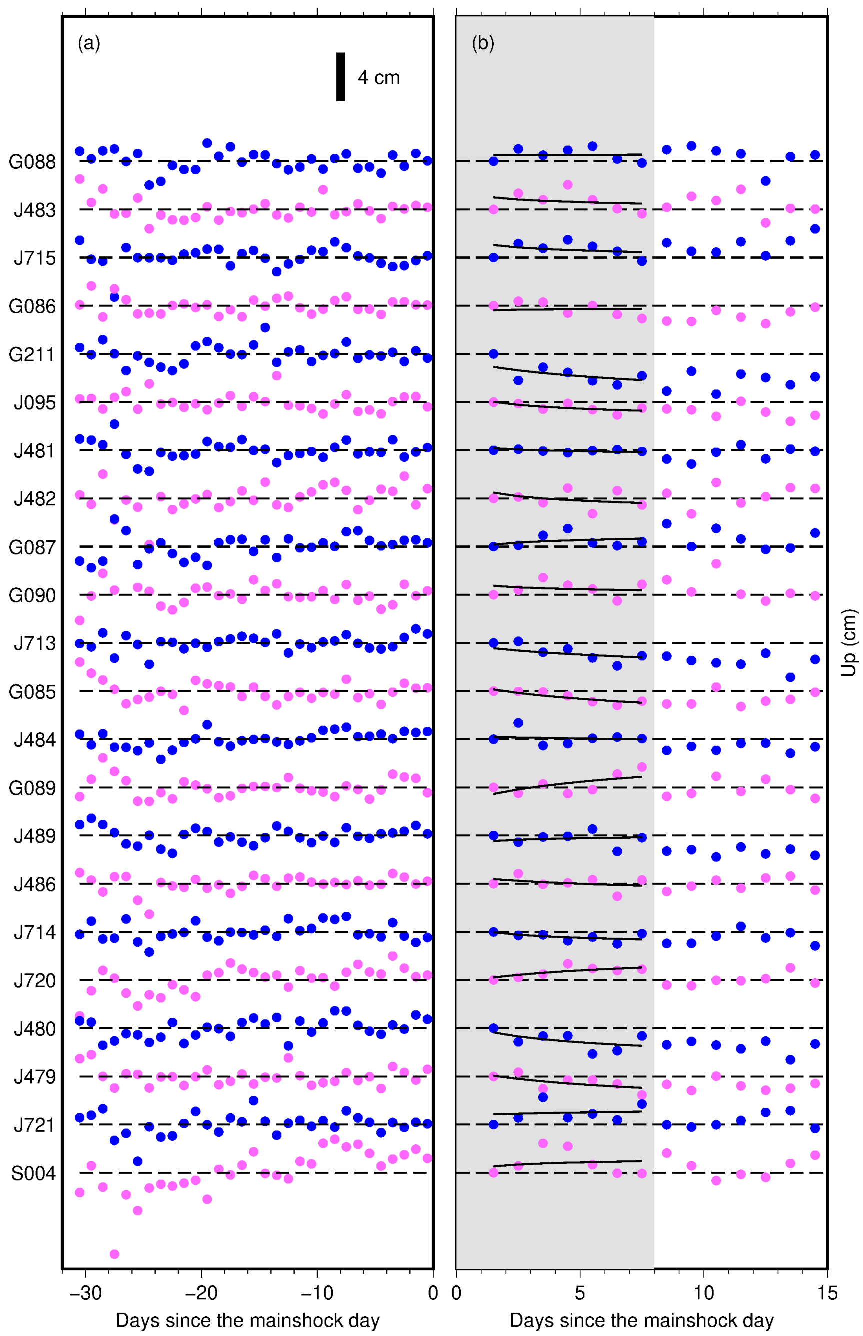

Figure S4. Same as Figure S2 but for the vertical component.

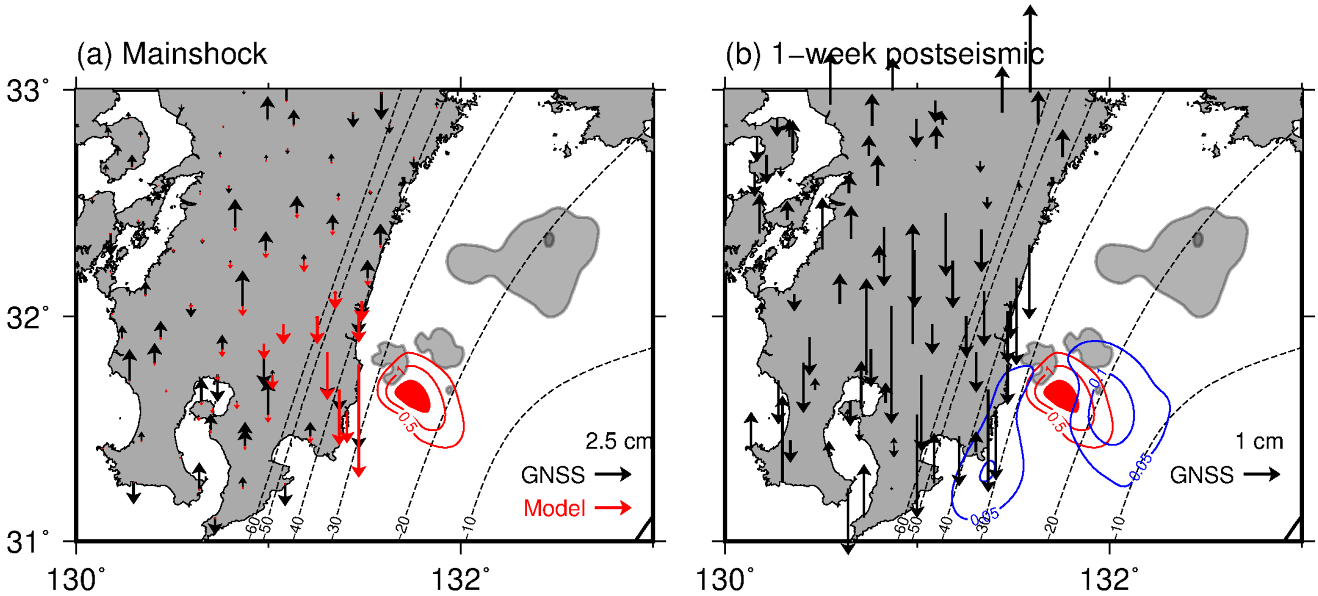

Figure S5. Coseismic (a) and 1-week postseismic (b) displacements. Refer to Figure 3 for other elements. No postseismic model displacements are drawn in (b) because we did not invert the vertical postseismic displacements. Refer to Figure 3 for other elements. Figure S7 shows the identical displacements with the error ellipses.

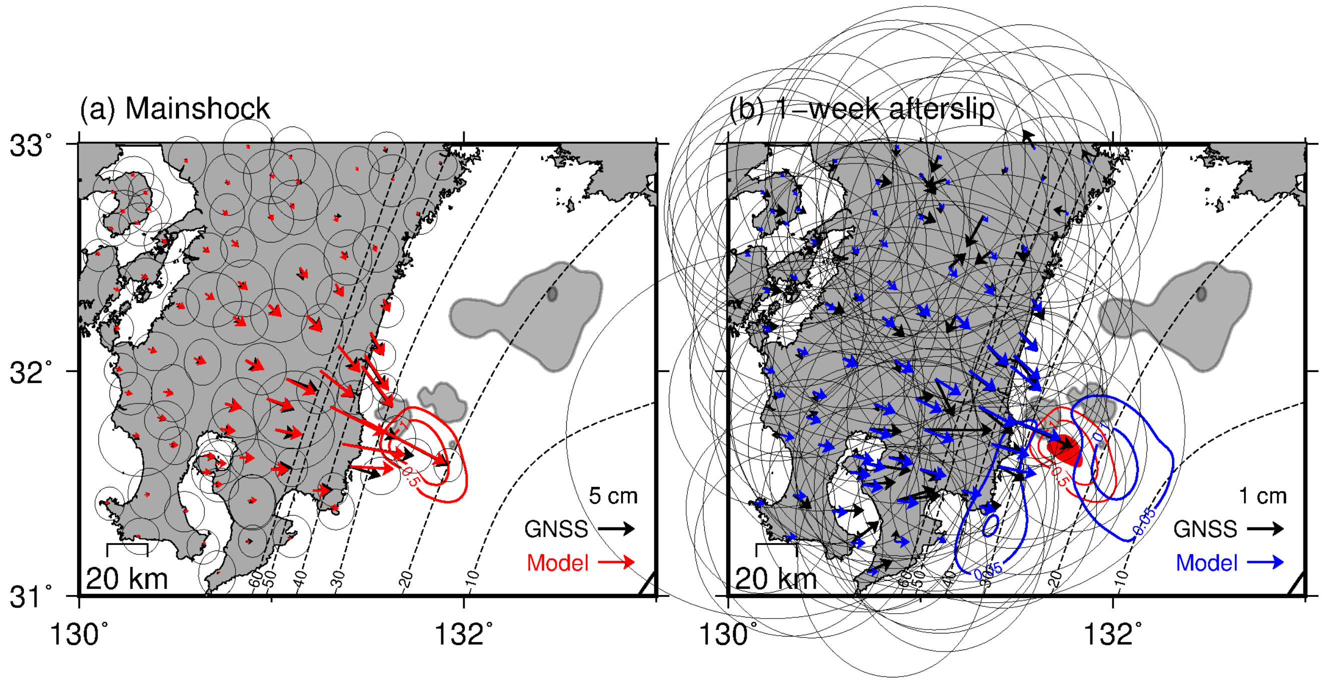

Figure S6. Horizontal co- (a) and post-seismic (b) displacements with 95% confidence ellipses. The displacements are identical to those shown in Figure 3a-b.

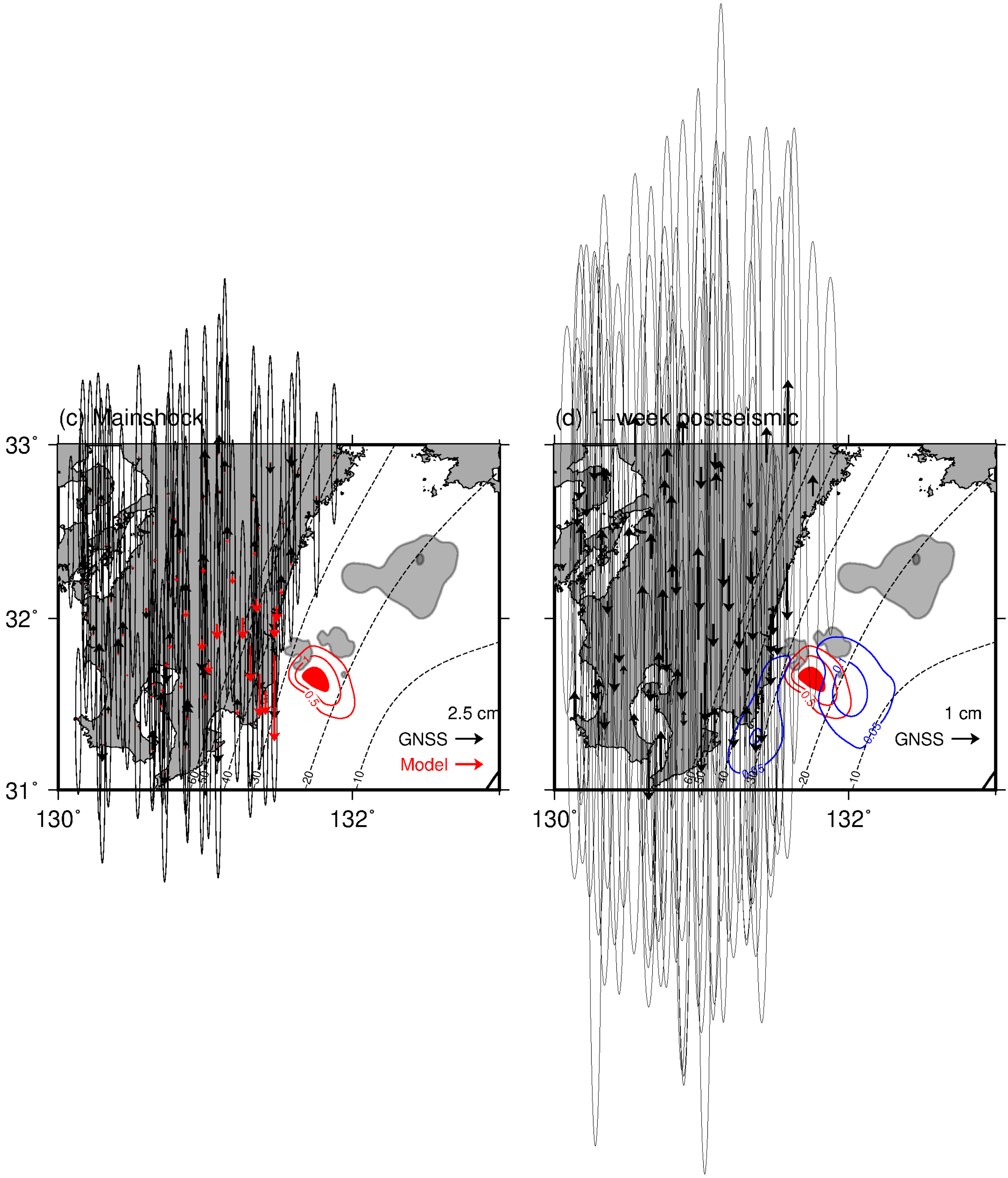

Figure S7. Vertical co- (a) and post-seismic (b) displacements with 95% confidence ellipses. The displacements are identical to those shown in Figure S5.

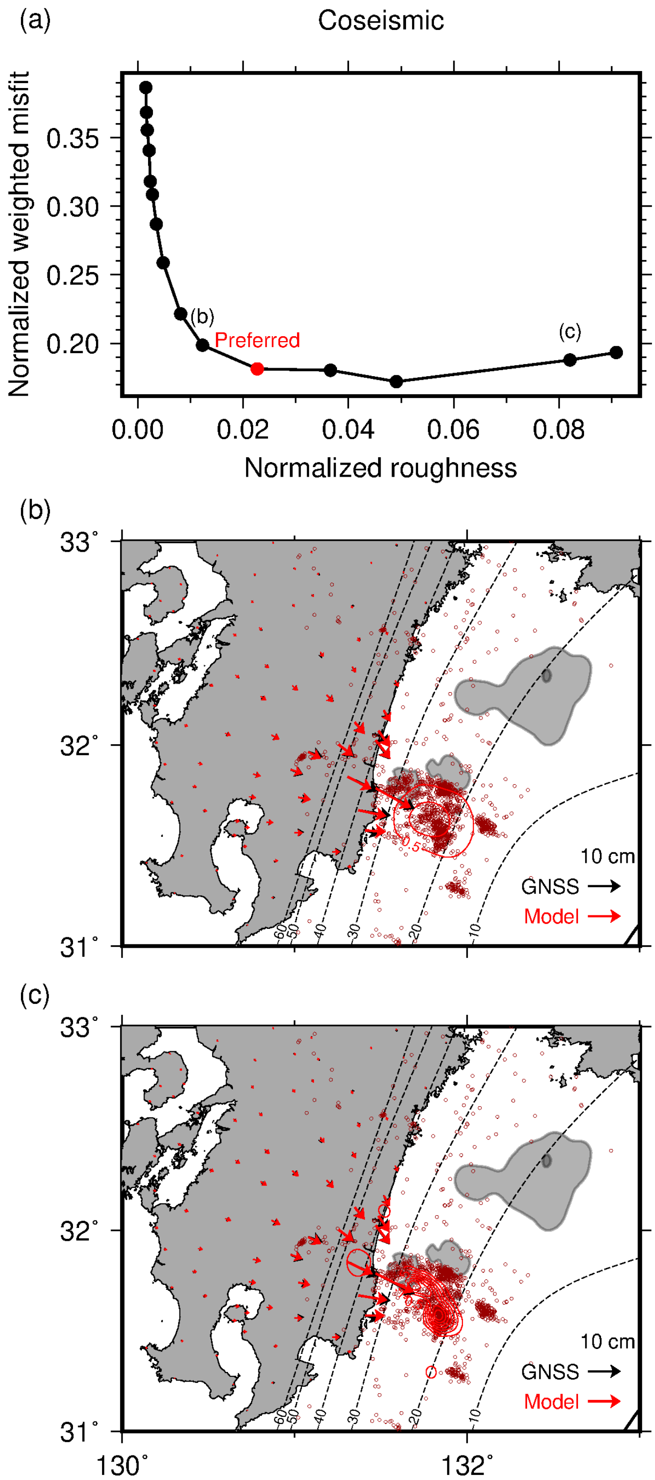

Figure S8. (a) Trade-off curve for the coseismic slip inversion. Horizontal and vertical axes indicate weighted misfit and roughness normalized by the sum of the data norm weighted by their nominal errors. The red dot indicates the preferred solution in Figure 3a. (b-c) Examples of smoother (b) and rougher (c) solutions. Refer to Figure 3 for other elements.

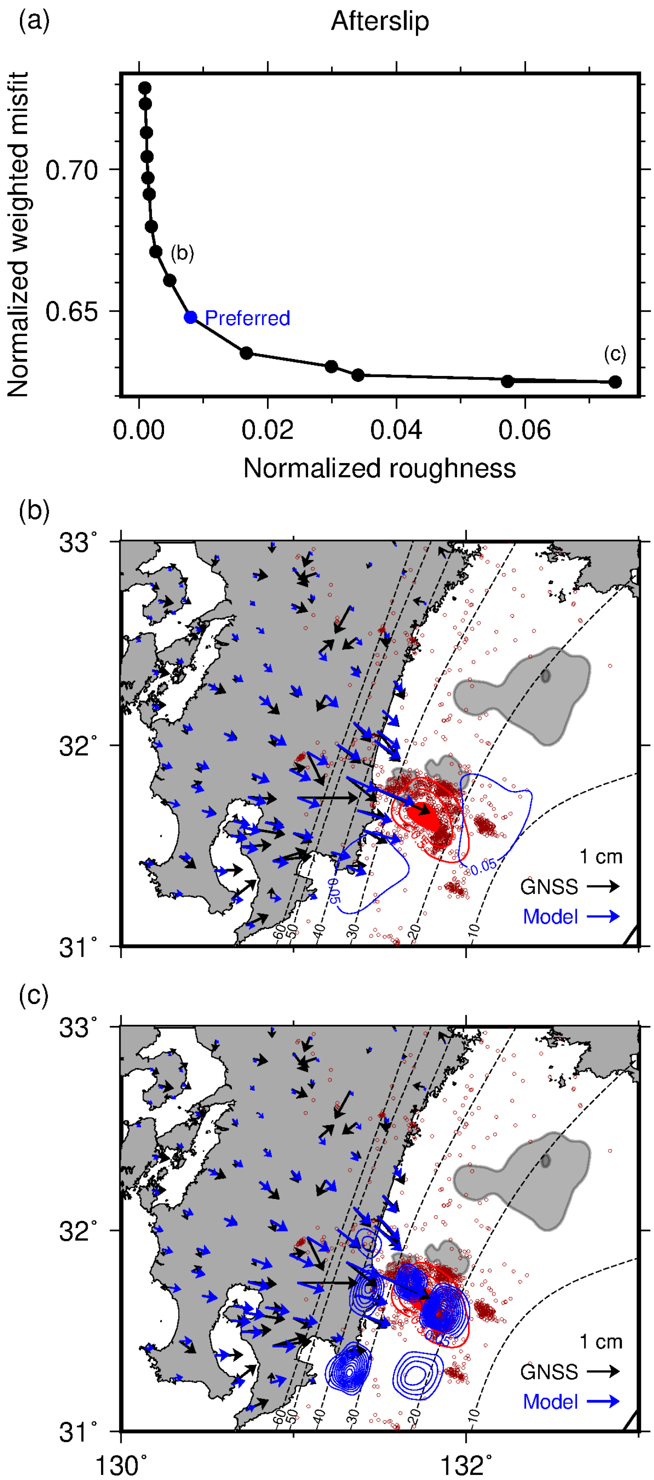

Figure S9. (a) Same as Figure S8 but for the afterslip inversion. The blue dot indicates the preferred solution in Figure 3b. (b-c) Examples of smoother (b) and rougher (c) solutions. Refer to Figure 3 for other elements.

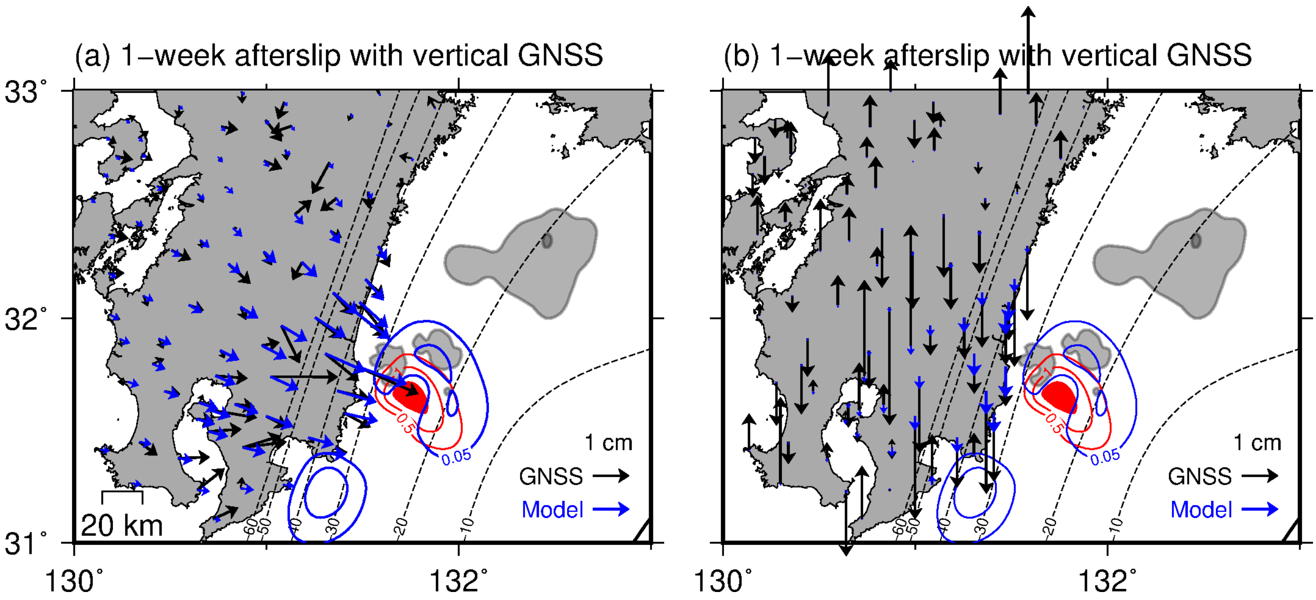

Figure S10. Afterslip inversion result with the vertical displacements with the identical setting as Figure 3a-b. Refer to Figure 3 for other elements.

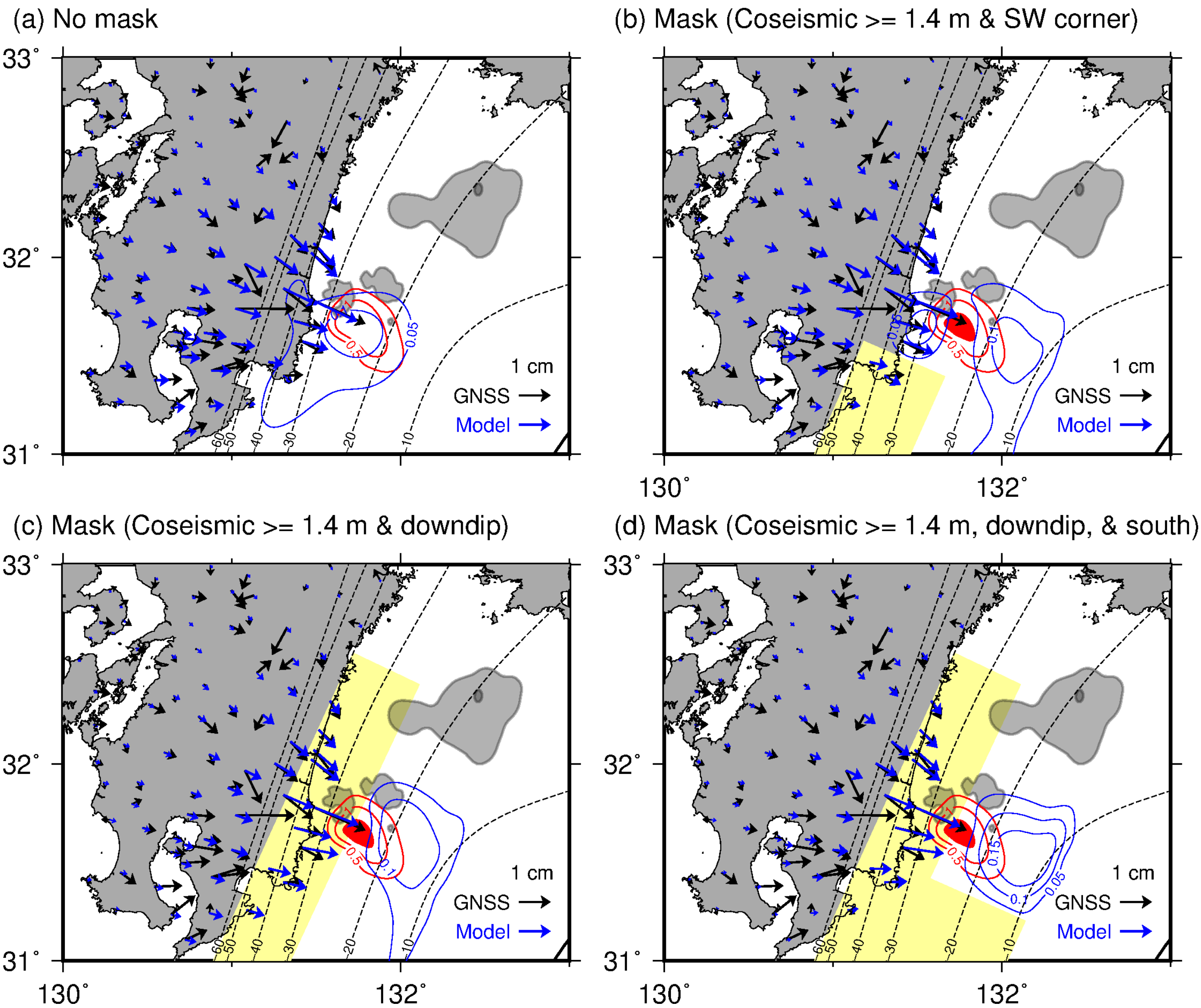

Figure S11. (a) The estimated 1-week afterslip distribution without any mask of slip area. (b-d) Same as (a) but slip in the area of the coseismic slip more than 1.4 m (filled in red) and the area highlighted in yellow is constrained to be zero. Refer to Figure 3 for other elements.

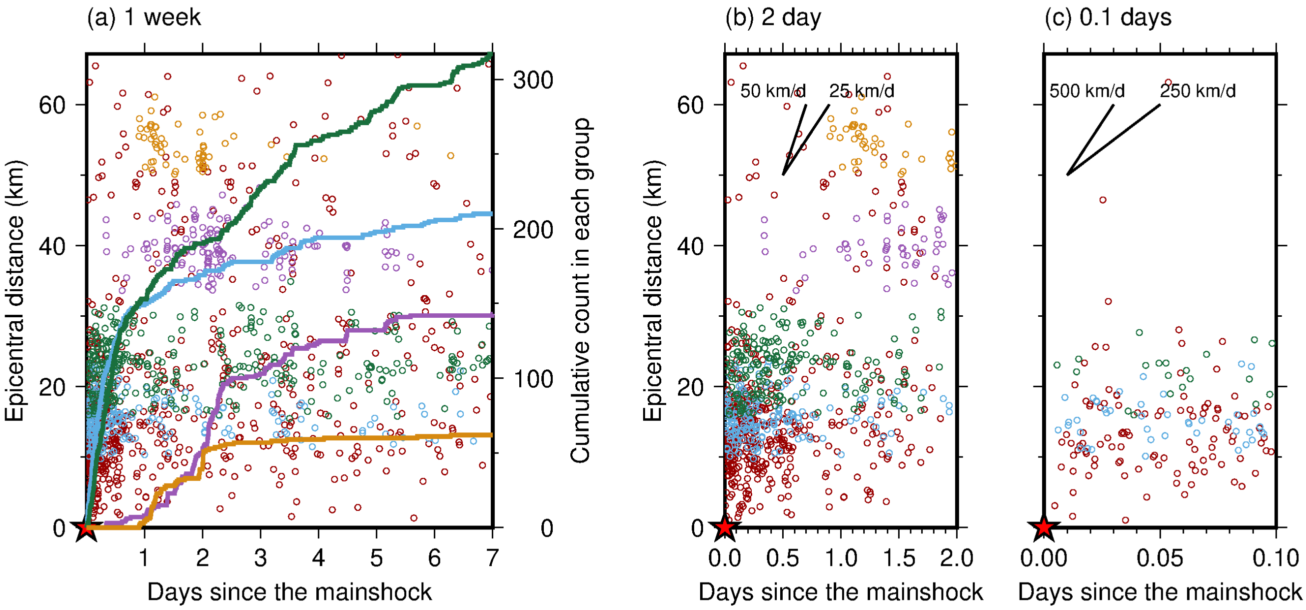

Figure S12. (a) Same as Figure 4b but with the time axis is linear. (b-c) Zoom-in for the first 2 (b) and 0.1 (c) days.

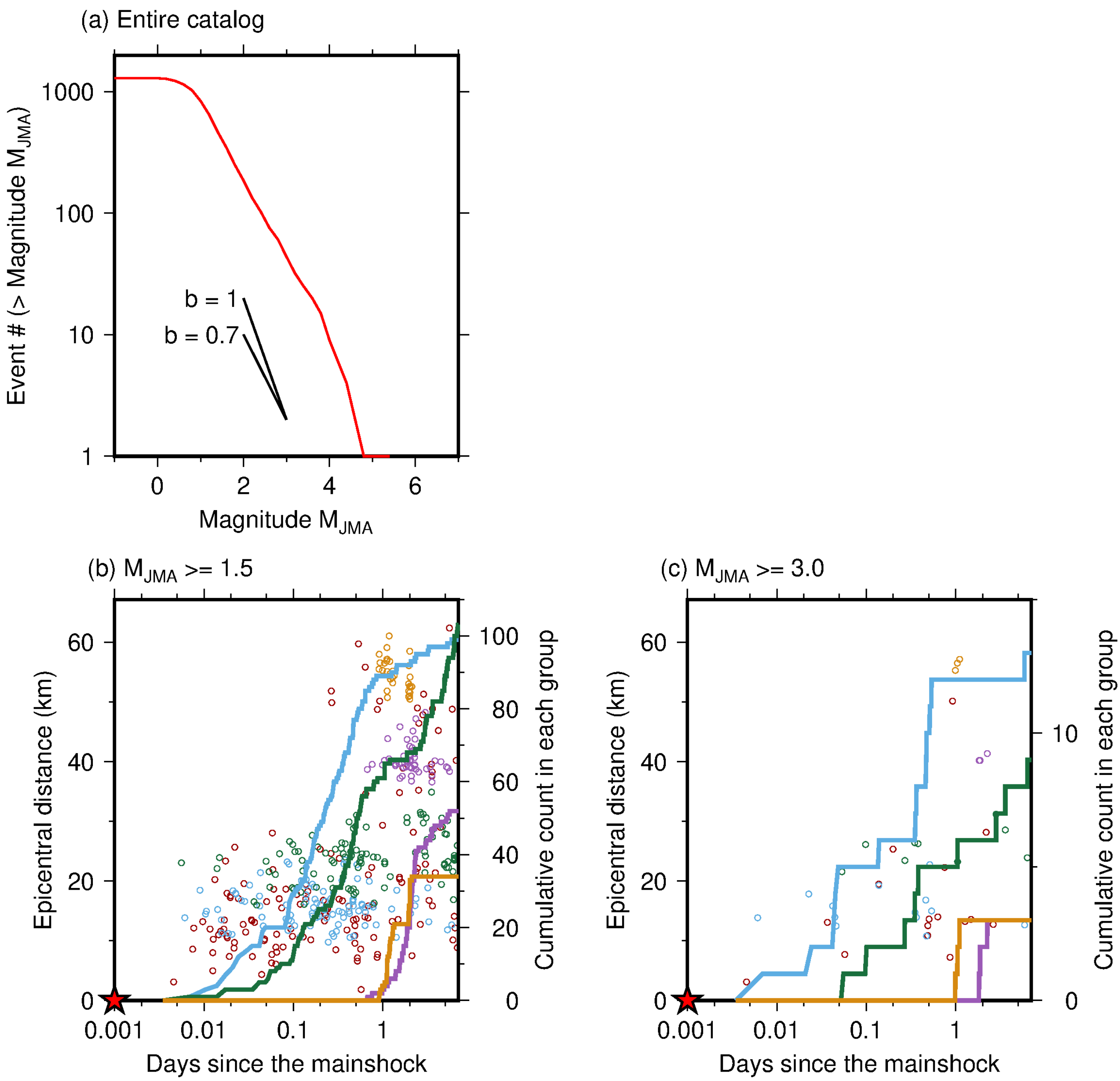

Figure S13. (a) The cumulative count of 1-week aftershocks against their magnitude M_{JMA}. The black lines indicate slopes corresponding to different b-values of the Gutenberg-Richter law. (b-c) Same as Figure 4b but with the 1-week aftershocks only above a given magnitude as labeled.

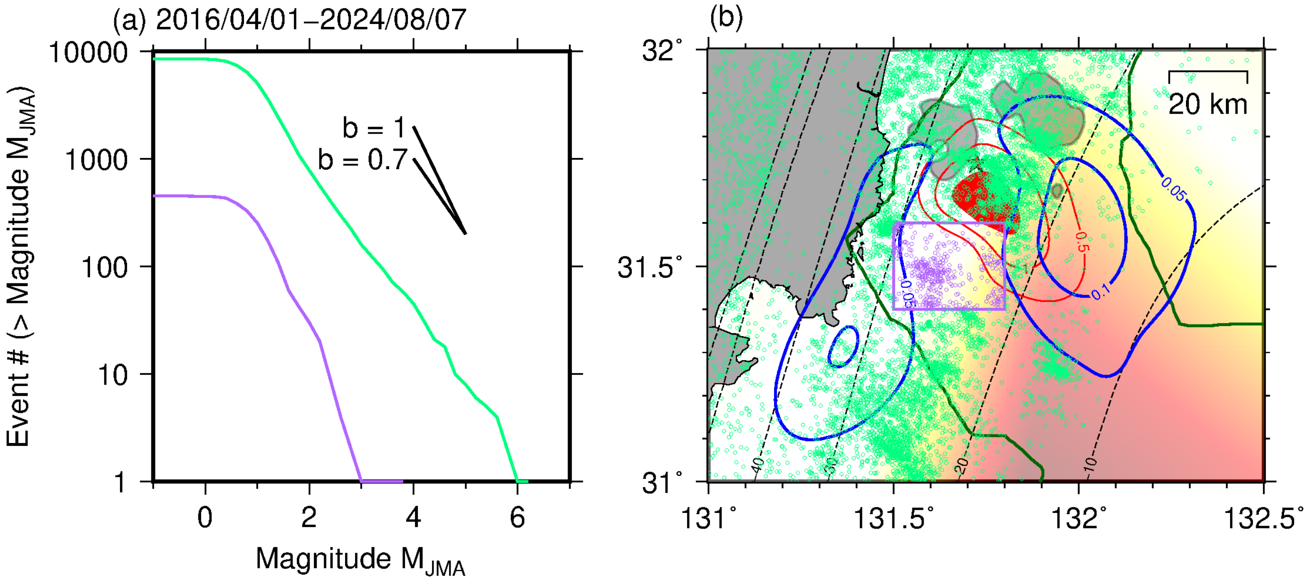

Figure S14. (a) The cumulative count of seismicity between April 1 2016 and August 7 2024 against their magnitude M_{JMA}. Green and purple curves indicate the distributions for the entire area and inside the purple box, respectively, in (b). We extracted events within 10 km from the slab interface. The black lines indicate slopes corresponding to different b-values of the Gutenberg-Richter law. (b) Seismicity between April 1 2016 and August 7 2024 (green and purple). See Figure 3c for the other elements.